Special Collection
Process Diagnostics for CMIP6

The Physics behind Precipitation Onset Bias in CMIP6 Models: The Pseudo-Entrainment Diagnostic and Trade-Offs between Lapse Rate and Humidity

TODD EMMENEGGER,[a] FIAZ AHMED,[a] YI-HUNG KUO,[a,b] SHAOCHENG XIE,[c] CHENGZHU ZHANG,[c] CHENG TAO,[c] AND J. DAVID NEELIN[a]

[a] *Department of Atmospheric and Oceanic Sciences, University of California, Los Angeles, Los Angeles, California*
[b] *Cooperative Institute for Modeling the Earth System, Program in Oceanic and Atmospheric Sciences, Princeton University, Princeton, New Jersey*
[c] *Lawrence Livermore National Laboratory, Livermore, California*

(Manuscript received 14 April 2023, in final form 31 October 2023, accepted 29 December 2023)

ABSTRACT: Conditional instability and the buoyancy of plumes drive moist convection but have a variety of representations in model convective schemes. Vertical thermodynamic structure information from Atmospheric Radiation Measurement (ARM) sites and reanalysis (ERA5), satellite-derived precipitation (TRMM3b42), and diagnostics relevant for plume buoyancy are used to assess climate models. Previous work has shown that CMIP6 models represent moist convective processes more accurately than their CMIP5 counterparts. However, certain biases in convective onset remain pervasive among generations of CMIP modeling efforts. We diagnose these biases in a cohort of nine CMIP6 models with subdaily output, assessing conditional instability in profiles of equivalent potential temperature, θ_e, and saturation equivalent potential temperature, θ_{es}, in comparison to a plume model with different mixing assumptions. Most models capture qualitative aspects of the θ_{es} vertical structure, including a substantial decrease with height in the lower free troposphere associated with the entrainment of subsaturated air. We define a "pseudo-entrainment" diagnostic that combines subsaturation and a θ_{es} measure of conditional instability similar to what entrainment would produce under the small-buoyancy approximation. This captures the trade-off between larger θ_{es} lapse rates (entrainment of dry air) and small subsaturation (permits positive buoyancy despite high entrainment). This pseudo-entrainment diagnostic is also a reasonable indicator of the critical value of integrated buoyancy for precipitation onset. Models with poor θ_e/θ_{es} structure (those using variants of the Tiedtke scheme) or low entrainment runs of CAM5, and models with low subsaturation, such as NASA-GISS, lie outside the observational range in this diagnostic.

KEYWORDS: Convection; Deep convection; Entrainment; Precipitation; Diagnostics

1. Introduction

a. Overview

Ill-constrained representations of deep clouds and precipitation are major contributors to uncertainty in global climate model (GCM) projections, including, but not limited to, precipitation extremes (Meehl et al. 2000; Allen and Ingram 2002; Trenberth et al. 2003; Pall et al. 2007; Schneider et al. 2010), the diurnal cycle of precipitation (Del Genio and Wu 2010; Rio et al. 2009; Hourdin et al. 2013; Covey et al. 2016; Xie et al. 2019; Tang et al. 2021, 2022), and the Madden–Julian oscillation (Del Genio 2012; Zhu and Hendon 2015; Kim et al. 2012). Entraining plume models and their underlying assumptions serve as the basis of most GCM convective schemes (e.g., Arakawa and Schubert 1974; Kain and Fritsch 1990; Zhang and McFarlane 1995; Chikira and Sugiyama 2010; Schiro et al. 2018), often relying on integrated measures of instability to initiate convective updraft and subsequent precipitation. The environmental (grid-scale) response to this instability is tethered to local convection (sub-grid-scale) through large-scale governing equations that are typically consistent with quasi-equilibrium assumptions—instability generated in the large scale is removed by convective heating (e.g., Manabe et al. 1965; Arakawa and Schubert 1974).

Thermodynamic profiles from Atmospheric Radiation Measurement (ARM) sites provide valuable information for

Denotes content that is immediately available upon publication as open access.

Supplemental information related to this paper is available at the Journals Online website: https://doi.org/10.1175/JCLI-D-23-0227.s1.

Corresponding author: Todd Emmenegger, temmen@atmos.ucla.edu

DOI: 10.1175/JCLI-D-23-0227.1

processes relevant to tropical clouds and their interaction with the large-scale environment. From the vertical structure of temperature and humidity, the potential for moist convection is assessed through relations of the equivalent potential temperature θ_e and equivalent saturation potential temperature θ_{es}. Being a conserved quantity under adiabatic lifting, θ_e profiles provide theoretical buoyancy measures of environments—similar to traditional meteorological metrics such as CAPE—with weighting of height levels emulating the entrainment process undergone by steady-state plumes (more details provided in section 4). This plume formulation, accompanied by simple entrainment assumptions, provides a framework for gauging model biases with respect to the onset of convection. Working toward a process-oriented diagnostic of convection—diagnostics that isolate a physical process, target related parameters in GCMs, and relay actionable feedback (Maloney et al. 2019)—we seek to condense these vertical structures of moisture and temperature using key metrics of entraining plume buoyancy. We are led to intermodel differences in the relationships among (i) the decrease with height of θ_{es} in the lower free troposphere (LFT), referred to as the θ_{es} lapse rate for brevity; (ii) the boundary layer θ_e; and (iii) the subsaturation (as measured by $\theta_e - \theta_{es}$) of the LFT. Building on prior theoretical work concerning quasi-equilibrium, we present a "pseudo-entrainment" process-oriented diagnostic. The pseudo-entrainment diagnostic is an estimation of entrainment under the bulk plume formulation that explains tradeoffs between tropical lapse rates (stability) and moisture. We term it the pseudo-entrainment diagnostic because even when assumptions do not hold well, it is a useful large-scale indicator of processes relevant to impacts of entrainment. Additionally, the pseudo-entrainment diagnostic helps identify convective onset biases—precipitation being initiated too early or late as represented by the "pickup" of precipitation.

b. Convective onset and the role of entrainment

The pickup in precipitation statistics, first identified on daily (Bretherton et al. 2004) and subdaily (Peters and Neelin 2006) time scales in which the conditionally averaged precipitation picks up sharply after a critical value of column relative humidity (CRH) is reached, represents the occurrence of conditional instability in the transition to deep convection (Holloway and Neelin 2009; Schiro et al. 2016). The pickup is observed over tropical land and ocean in observational records (Neelin et al. 2009; Ahmed and Schumacher 2017; Schiro 2017) and models (Kuo et al. 2020) and has been used in GCM evaluation in CMIP5 (Rushley et al. 2018) and CMIP6 (Emmenegger et al. 2022) models. The precipitation–CRH relationship reflects the effects of entrainment on the buoyancy of convective plumes (Holloway and Neelin 2009). The importance of the lower-free tropospheric (LFT) moisture in this regard is well established and is reflected in the pickup (Kuo et al. 2018; Bretherton et al. 2004; Ahmed and Schumacher 2015; Neelin et al. 2009).

Considerations of entrainment/dilution of CAPE have led to more realistic representations of convective processes in models (Zhang 2009); lack of entrainment can render models unable to reproduce convective variability across subdaily to interannual time scales (Tokioka et al. 1988; Neale et al. 2008; Del Genio and Wu 2010; Kim et al. 2012). More recently, measures of LFT buoyancy have expanded on the relationship between the entrainment process and precipitation (Ahmed and Neelin 2018; Ahmed et al. 2020; Adames et al. 2021; Ahmed and Neelin 2021a; Wolding et al. 2020, 2022). Specifically, observed mass flux profiles and vertical velocities imply substantial entrainment of environmental air through the lower free troposphere (Kumar et al. 2015; Giangrande et al. 2016; Schiro et al. 2018). Observational field campaigns (Yeo and Romps 2013) and modeling studies (McGee and van den Heever 2014) point to organized flow in mesoscale convective systems, with a substantial LFT inflow into the convective updraft. Signatures of heavy entrainment inspired the deep-inflow formulation of mixing in Holloway and Neelin (2009), which has proven useful in estimating convective instability (similar to the GCM formulation of entraining CAPE) and is used in this study.

Conditioning precipitation on a form of entraining CAPE (theoretical buoyancy of an entraining plume) proves more successful than the traditional measure of CAPE stemming from the nonmixing assumption in predicting convection [shown in section 5c herein and in Adames et al. (2021) and Ahmed and Neelin (2021a)]. However, estimating the exact degree of entrainment undergone by a convective plume from observational products remains a complex problem. Attempts at estimating entrainment rates often requires knowledge of cloud-top height from observational snapshots (Luo et al. 2010; Jensen and Del Genio 2006) or additional assumptions of the degree to which the plume is reflected in the environmental profile.

c. Small buoyancy approximation

Such estimations of plume trajectories depend on the environment, but also interact with it. The concept of convective adjustment posits that convection acts to remove convective instability by adjusting the nonconvecting large-scale environment (Manabe and Strickler 1964; Arakawa and Schubert 1974), assuming that gravity waves quickly homogenize temperature anomalies in the free troposphere (Sobel and Bretherton 2000; Bretherton and Smolarkiewicz 1989) or that the large-scale environment adjusts to anomalous temperature introduced by the plume. Convective adjustment is employed as a closure in several convective schemes (Manabe and Strickler 1964; Manabe et al. 1965; Betts 1986; Betts and Miller 1986; Keil et al. 2014) and is generalized as convective quasi-equilibrium (e.g., Arakawa and Schubert 1974; Emanuel et al. 1994). The adjustment process is assumed to happen instantaneously or with a finite adjustment time scale (Moorthi and Suarez 1992; Zhang and McFarlane 1995; Bechtold et al. 2008; Ahmed et al. 2020). The exact measure of instability can vary among implementations, with CAPE and the cloud-work function being common choices. A time scale separation between the slow buildup of instability and fast adjustment by convection results in a state of quasi-equilibrium (QE; Neelin et al. 2008; Yano and Plant 2012).

With the QE framework in mind, the adjustment of the vertical profile of environmental temperature to that of a bulk convective plume places further emphasis on the entrainment

process, mainly that the lapse rate of the environment during raining times reflects the rate of dilution of a bulk plume. In simple terms, whether the entrainment is turbulent or coherent, the effects of entrainment rely on two factors, 1) the fraction of environmental air incorporated into the plume (entrainment rate) and 2) the saturation deficit of the environmental air being entrained (the two factors can compensate to achieve the same amount of dilution of a parcel such as high entrainment of moist air or low entrainment of dry air). QE predicts that the temperature and moisture profiles in the tropics reflect this process of entrainment—not just in strongly convective plumes but in the aggregate effect of the ensemble of all tropical convection (Singh and O'Gorman 2013; Singh et al. 2019; Bao et al. 2021; Bao and Stevens 2021; Singh and Neogi 2022).

The *small buoyancy approximation*—the approximation that buoyancy is minimized as the environment adjusts to anomalous temperatures introduced by the plume—applies if the convective adjustment time scale is sufficiently fast. The leading-order approximation has the large-scale temperature and moisture profile adjusted to that of the convection (zero buoyancy), while the precipitation and other convective effects occur due to the small departures from this (e.g., Neelin and Yu 1994; Neelin and Zeng 2000). The leading-order (small buoyancy) approximation can be used to estimate radiative-convective equilibrium temperature and moisture profiles (Singh and O'Gorman 2013; Zhou and Xie 2019) and provides a method for consistently treating departures from zero buoyancy associated with raining events (e.g., Ahmed et al. 2020). In section 7, we derive the pseudo-entrainment diagnostic, an estimate of entrainment undergone by a bulk plume through the LFT, by applying the small buoyancy approximation to thermodynamic profiles of the environment.

d. Diagnostics from moist thermodynamic profiles

Due to this interaction, tropical atmospheric temperature and moisture profiles reflect the processes contributing to plume buoyancy: nonentraining aspects of conditional instability are captured by atmospheric boundary layer (ABL) moist entropy relative to LFT temperature (measured by saturation moist entropy) and dilution and entrainment are seen in the dependence on moistening of the LFT. In convective scheme formulations, the convective trigger requires a degree of preconditioning—moistening and warming of ABL along with moistening and cooling of LFT—and with it, an associated magnitude of instability. For instance, the larger the effect of entrainment, the greater the amount of preconditioning required for convection to initiate, and the larger the convective onset threshold. We build on previous observational work, framed in terms of deep convective inhibition (Raymond et al. 2003; Raymond 2017; Fuchs-Stone et al. 2020) and the instability index (Raymond et al. 2011; Gjorgjievska and Raymond 2014) that finds relations between measures of LFT lapse rates of saturation moist entropy, boundary layer entropy, and precipitation rates. In this study, we explore and quantify the existence of an intricate balance of lapse rates, entrainment, and climatological moisture which coalesce to form the tropical climatology to identify strengths and shortcomings in model representations of these processes.

In section 3 we present a measure of LFT buoyancy based on the equivalent potential temperature definition. In section 4 we describe our plume model which allows us to calculate a scalar quantity of the average LFT parcel buoyancy, B_L, with inputs of vertical profiles of moisture, temperature under various mixing assumptions. The convective transition statistics conditioned on B_L are presented in section 5c. Biases identified here are then further explored in an analysis of the vertical structures associated with different B_L regimes in sections 5 and 6. In section 7, we conclude with the derivation of the pseudo-entrainment diagnostic, a bulk estimation of the entrainment rate from the average raining profiles, and apply this diagnostic to both models and observations.

2. Data and model descriptions

The thermodynamic structures associated with convection and their representation in global climate models (GCMs) are evaluated at the Nauru ARM site in the tropical western Pacific (0°31′S, 166°54′E) for the period 1999–2009. Surface precipitation rate and vertical profiles of humidity and temperature from the ARM Best Estimate dataset (ARMBE; Xie et al. 2010), an hourly integrated product assembled from various in situ ARM measurements, provides an observational baseline for GCM evaluation. The hourly fifth-generation European Center for Medium-Range Weather Forecasts (ECMWF) reanalysis product (ERA5; Hersbach et al. 2020) provides an additional baseline for GCM evaluation. Satellite retrieval Tropical Rainfall Measuring Mission (TRMM) 3b42 version 7 precipitation measurements (Tropical Rainfall Measuring Mission 2011) provide an additional precipitation product to augment with column variables. For the purpose of model evaluation, the TRMM 3B42 precipitation is averaged spatially over 1° from its 0.25° × 0.25° resolution, centered on the latitude–longitude point nearest to the sites.

Output from nine ocean–atmosphere coupled GCMs' historical experiment of the CMIP6 are analyzed. A summary of each model: its resolution and convective trigger/closure are shown in Table 1. For each model, we extract 6-hourly vertical profiles of temperature and moisture and 3-hourly averaged surface precipitation rate at the nearest grid point to the Nauru site over the years 1995–2015 of the CMIP6 historical experiment. Models were chosen by the availability of subdaily humidity, temperature, and precipitation at the time of the analysis. Precipitation data for NASA-GISS, MPI-ESM1-2-LR, MIROC-E2SL, MIROC6, MRI-ESM2-0, NESM3, is 3-hourly averaged, while MPI-ESM1-2-HAM, NorESM2-LM, and NorESM2-MM output is 6-hourly averaged. Vertical profiles for both observations and models are instantaneous snapshots. The start of the precipitation averaging window is aligned with these snapshots so that profiles of temperature and moisture lead precipitation. Vertical profiles will be used to calculate measures of lower free tropospheric buoyancy (a measure of instability similar to entraining CAPE) and are considered causal to moist convection and precipitation.

To test the efficacy of the pseudo-entrainment diagnostic, the CMIP6 models are supplemented with an additional set of

TABLE 1. List of models analyzed in this study. This table is nearly identical to Table 1 of Emmenegger et al. (2022). The references column gives the data source and the source for the convective trigger/closure.

Model name	Institute	Resolution (lon × lat), vertical levels	Convective trigger/closure	References
NASA-GISS	Goddard Institute for Space Studies, NASA	2.00° × 2.00°, 40	Higher moist static energy of an adiabat to environment at level above/cloud-base buoyancy	NASA Goddard Institute for Space Studies (2018), Del Genio and Yao (1993), Schmidt et al. (2014)
MPI-ESM-1-2-HAM	Max Planck Institute for Meteorology	1.85° × 1.88°, 47	Net positive moisture convergence/CAPE	Wieners et al. (2019), Möbis and Stevens (2012)
MPI-ESM1-2-LR	Max Planck Institute for Meteorology	1.85° × 1.88°, 47	Net positive moisture convergence/CAPE	Wieners et al. (2019), Möbis and Stevens (2012)
MIROC-E2SL	Japan Agency for Marine-Earth Science and Technology	2.77° × 2.81°, 40	CAPE/prognostic convective kinetic energy	Hajima et al. (2019), Ando et al. (2021)
MIROC6	Japan Agency for Marine-Earth Science and Technology	1.39° × 1.41°, 81	CAPE/prognostic convective kinetic energy	Tatebe and Watanabe (2018), Ando et al. (2021)
MRI-ESM2-0	Meteorological Research Institute Japan Meteorological Agency	1.11° × 1.13°, 80	CAPE/CAPE	Yukimoto et al. (2019, 2011)
NorESM2-LM	Norwegian Meteorological Institute	1.89° × 2.50°, 32	CAPE/CAPE	Seland et al. (2019, 2020)
NorESM2-MM	Norwegian Meteorological Institute	0.94° × 1.25°, 32	CAPE/CAPE	Bentsen et al. (2019), Seland et al. (2020)
NESM3	Nanjing University of Information Science and Technology	1.85° × 1.88°, 47	Net positive moisture convergence/CAPE	Cao and Wang (2019), Cao et al. (2018)
CAM5	National Center for Atmospheric Research	0.90° × 1.25°, 27	CAPE/CAPE	Neale et al. (2010)

perturbed-physics experiments using the Community Atmospheric Model version 5 (CAM5; Neale et al. 2010). Two-year atmosphere-only simulations with fixed sea surface temperatures are run. The entrainment rates in the Zhang–McFarlane cumulus parameterization scheme (Zhang and McFarlane 1995) are perturbed over a range of values: 0.25, 0.5, 0.75, 1 (control), and 1.25 km^{-1}. An additional case where the convective parameterization is turned off is also included.

3. A measure of lower free tropospheric buoyancy B_L

Buoyancy here is written as

$$B = g\left(\frac{\delta\theta_{es}}{\kappa\theta_{es}} + 0.61\delta q_v - \delta q_c\right), \tag{1}$$

where θ_{es} is saturated equivalent potential temperature, δ represents the difference between the plume and the environment, with θ_{es}^{p} that of the parcel and θ_{es} without the superscript is that of the environment; q_v is the water vapor mixing ratio, q_c is the condensate mixing ratio, and g is the acceleration due to gravity. The factor

$$\kappa = 1 + \frac{L^2 q_s}{c_p R_v T_0 T} \tag{2}$$

arises when converting from the temperature-based form of buoyancy (Adames et al. 2021; Raymond 1994, and in the online supplemental material). In Eq. (2), L is the latent heat of vaporization, q_s is the saturation specific humidity of the environment, c_p is the specific heat of dry air, R_v is the gas constant of water vapor, and T_0 is a constant reference temperature.

The second and third terms represent the contributions from 1) the water vapor effect on density (sometimes called the virtual effect, incorporated in the definition of virtual temperature) and 2) condensate loading.

Rewriting (1) provides a convenient way of comparing a slightly modified curve corresponding to θ_{es} from a plume calculation to the θ_{es} of the environment, such that the distance between these curves is proportional to buoyancy, including the virtual effect and condensate loading:

$$B = \frac{g}{\kappa\theta_{es}}\left[\underbrace{\theta_{es}^{p} + \overbrace{\kappa\theta_{es}(0.61\delta q_v - \delta q_c)}^{\text{virtual effect}-\text{condensate loading}}}_{\text{compare to } \theta_{es}} - \theta_{es}\right]. \tag{3}$$

Note that virtual effect and condensate loading quantities are not conserved under parcel motion. The measure of plume buoyancy in (1) is similar to that used in Raymond (1994) and Adames et al. (2021) and differs from the measure used in Ahmed and Neelin (2018) in that the κ factor is included in the denominator. As noted in Adames et al. (2021), the inclusion of κ does not significantly affect the results of Ahmed and Neelin (2018) and Adames et al. (2021) but serves to scale

TABLE 2. Values of constant used for the buoyancy calculation in Eq. (1).

Variable	Description	Value	Units
g	Acceleration due to gravity	9.8	m s^{-2}
L	Latent heat of vaporization	2.5	$\times 10^6$ J kg^{-1}
c_p	Specific heat capacity of dry air	1005	J kg^{-1} K^{-1}
R_v	Gas constant for water vapor	461	J kg^{-1} K^{-1}
T_0	Reference temperature	300	K
p_0	Reference pressure	1000	hPa

the numerator to values ~3 times smaller. Values of the constants used in this study are displayed in Table 2. Equivalent potential temperature θ_e is the temperature a parcel would attain after a moist adiabatic expansion to a low pressure, followed by an adiabatic compression to a reference pressure. It is approximately conserved in both moist and dry adiabatic reversible processes. Variables based on θ_e are more useful in approximating the conservation properties of a plume than moisture and temperature (Ahmed and Neelin 2018).

To interpret Eq. (1), we now express a typical parcel lifting trajectory using θ_e-based variables. A near-surface unsaturated parcel is lifted and conserves its potential temperature θ, up until it becomes saturated at its lifting condensation level (LCL; where $\theta_e^p = \theta_{es}^p$). The parcel remains saturated in its ascent above the LCL with $\theta_e^p = \theta_{es}^p$.

The level of free convection (LFC) is where $\theta_e^p = \theta_{es}^p$. The lifting condensation level is below the LFC for a lifted parcel with no mixing assumptions, assuming the lapse rate of the environment is less than that of a dry adiabat. In a well-mixed atmospheric boundary layer, there is typically some convective inhibition below the LFC, as noted in Raymond (1994).

4. Plume calculation description

In our plume calculations, we assume the bulk plume undergoes reversible moist-adiabatic transitions allowing for ice, conserving its equivalent potential temperature θ_e, calculated according to Eq. (2.67) in Stevens and Siebesma (2020), throughout its ascent. Further technical details of mixing may be found in Holloway and Neelin (2009); we provide a short summary here.

The bulk plume model takes the environmental profiles of temperature and moisture, and mixing coefficients as inputs. Mixing coefficients are prescribed and thermodynamic profiles are spline interpolated to 5-hPa intervals. A parcel originating from (with same temperature and moisture content) a near-surface level of the environment (in our calculations we choose a parcel at 1000 hPa) is lifted and interacts with the environment according to the prescribed mixing scheme in its ascent.

In the absence of mixing and precipitation, the total water content is conserved and undergoes phase changes 1) when the parcel reaches saturation below the freezing level (water vapor condenses to liquid), 2) when the freezing level is reached (liquid water is converted into ice)—during the freezing process the temperature is held at the triple point, allowing liquid and ice to coexist—and 3) when, above the freezing level, ice is formed via deposition of water vapor (supercooled water is not permitted in this equilibrium calculation). The total water content is conserved until the condensate reaches a cap of 1 g kg^{-1} and then is lost irreversibly as in Schiro et al. (2018).

Plume calculations are carried out for two different mixing assumptions: a nomixing case (NMX) and a heavy mixing case, "Deep Inflow B" (DIB; Holloway and Neelin 2009), which corresponds to convective plumes that entrain approximately equal amounts of air from each level in the lower troposphere. These two mixing assumptions probe the two extreme possibilities for entrainment behavior. The NMX case plume involves lifting a parcel originating near the surface (in all calculations we assume the plume starts at 1000 hPa) such that it conserves its θ_e throughout its ascent.

The DIB case is calculated by assuming an approximately linearly increasing updraft velocity at low levels which incorporates environmental air such that it can be approximated as an average of the layers below (Holloway and Neelin 2009; Schiro et al. 2016, 2018; Adames et al. 2021):

$$\theta_e^{\mathrm{DIB}}(p) \approx (p_s - p)^{-1} \int_{p_s}^{p} \theta_e(p')dp'. \tag{4}$$

From these plume values, we calculate buoyancy as presented in (5). To obtain a scalar value for statistical purposes, we average the lower tropospheric average buoyancy B_L and define it as

$$B_L = (p_s - p_{\mathrm{LFT}})^{-1} \int_{p_s}^{p_{\mathrm{LFT}}} B dp, \tag{5}$$

where the integrand B is determined for plume θ_{es}^p from each mixing scenario in (1).

The definition of B_L in (5) is similar to that previously used (Ahmed and Neelin 2018, 2021a; Adames et al. 2021; Wolding et al. 2022) and contains both negative and positive contributions similar to the traditional measure of convective available potential energy (CAPE) and convective inhibition (CIN). Measures of lower tropospheric buoyancy below the freezing level give the leading order behavior of a deep convection, as a convective plume needs to reach the freezing level to initiate deep convection (Stevens et al. 2017; Ahmed and Neelin 2018; Powell 2022). The average in (5) is taken from the surface to the top of the lower free troposphere, 600 hPa (just below the freezing level).

The primary difference between earlier uses of B_L and the one we present here is that we account for virtual effects and condensate loading in B. Virtual effects are sometimes neglected, but their contributions to buoyancy are not necessarily small (e.g., Sarachik 1985; Emanuel 1994; Holloway and Neelin 2009; Yang et al. 2022). From the arguments of the plume model and the definition of buoyancy in Eq. (1), the virtual contributions of vapor tend toward increasing buoyancy as the plume is at saturation above the boundary layer. Condensate loading effects can likewise be substantial (Bacmeister et al. 2012; Xu and Randall 2001), limited by entrainment and by precipitation processes that remove condensate from the

parcel. Here the microphysics of precipitation is simplified to a prescribed condensate cap. This limits the condensate loading to realistic values (Xu and Randall 2001; Neale et al. 2010). The environment can be assumed to be condensate-free, so $\delta q_c \approx q_c$ of the plume. Its maximum contribution to B is gq_c, so that with a condensate cap of 1 g kg^{-1}, the condensate contribution to B is approximately -1×10^{-2} m s^{-2}. Increasing the condensate cap can result in a significant drop in B_L. The vapor effect contribution remains relatively small $\sim 1 \times 10^{-2}$ m s^{-2}.

5. Key profile properties and buoyancy estimation

a. *Example profile*

Plume calculations are applied to all environmental snapshots of temperature and moisture. An example of the plume calculations and the environmental values of equivalent potential temperature is shown in Fig. 1. The freezing of plume liquid water may be identified by the kink in the trajectory of the plume θ_e (dashed lines) around 500 hPa (more pronounced in the NMX case (orange dashed) in Fig. 1 in both panels. The gradual increase of θ_e with height in the NMX case in Fig. 1 occurs due to the loss of condensate (after reaching the 1 g kg^{-1} cap slightly above the LCL). The shedding of condensate lends the parcel a decreased heat capacity, and continued freezing via vapor deposition and latent heat of fusion heat the parcel. The θ_{es} of the plumes [used to calculate buoyancy as in Eq. (1)] has the virtual and condensate loading contributions of buoyancy added in Fig. 1 according to the RHS of (3). The contributions are net positive for most of the lower troposphere (as seen by the difference between the parcel solid and dashed curves), albeit small (~1 K) and mostly reflect the shape of the θ_e profile of the environment—that is, the effect is greatest in those layers where the θ_e is low.

b. *Profiles averaged for raining events*

Figure 2 shows the plume and environmental profiles averaged over raining events (when precipitation rate $\geq$ 0.5 mm h^{-1}). In ARMBE and ERA5 the average DIB profile (Figs. 2a,b; red line) exhibits negative buoyancy throughout the LFT. This is also the case for the MPI models (Figs. 2d,e), In some models, during a raining event, the DIB profile shows positive buoyancy at a low level (~900–800 hPa) due to peak in θ_{es} (Figs. 2f–j) Only in the NASA-GISS model (Fig. 2c) does the DIB plume have positive buoyancy throughout the entire LFT. Nonentraining CAPE can be compared among models by the difference between the NMX plume (Fig. 2, orange line) and the θ_{es} (black). This difference compares the boundary layer θ_e and the lapse rate of θ_{es}. The MPI models and NESM3 exhibit small differences between their NMX plume and their θ_{es} profile, while NASA-GISS, MRI-ESM2-0, and the NorESM2 models show stark differences.

Figure 2 shows that the NMX and DIB profiles bound the model environmental θ_{es} profiles. At the leading order, the plume θ_{es} is expected to set the environmental θ_{es} profile based on convective adjustment arguments (small-buoyancy and WTG as outlined in section 1c; see also Singh and O'Gorman 2013; Zhou and Xie 2019). Models with strongly entraining convective schemes are expected to have θ_{es} profiles closer to

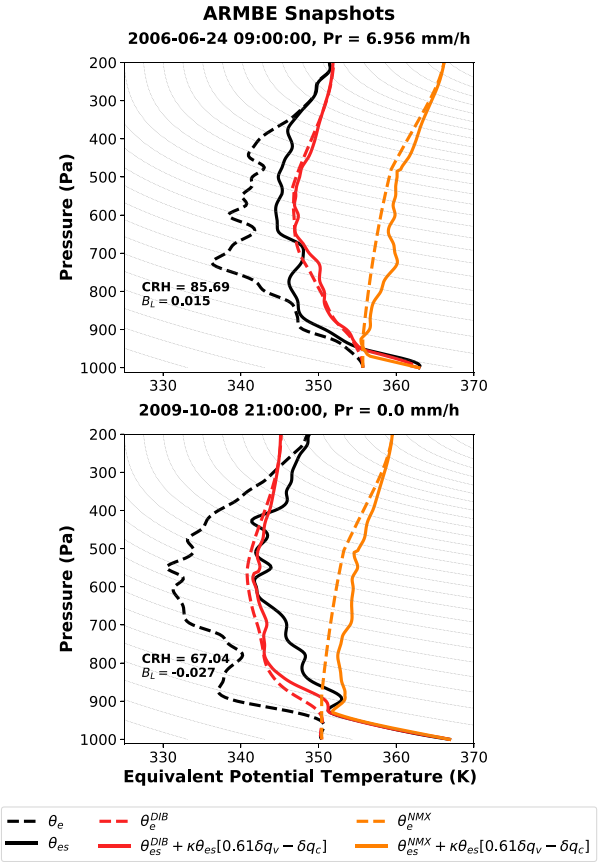

FIG. 1. Examples of the plume model calculations in the ARMBE dataset. Dashed lines represent the θ_e of the environment (black), the DIB-mixing plume (red), and the nonmixing plume (orange) with a condensate cap of 1 g kg^{-1}. The black solid line represents the θ_{es} of the environment, while the solid lines for the plume calculations give $\theta_{es}^p + \kappa\theta_{es}(0.61\delta q_v - \delta q_c)$. Parcel buoyancy (including virtual effects and condensate loading) is positive when this exceeds environmental θ_{es} per (3). Gray contours are lines of constant potential temperature. (top) An example of an individual sounding for a precipitating case, and (bottom) an example for a nonraining case. Note that equivalent potential temperature on the x axis is defined for reversible processes.

DIB, while models with weak entrainment are expected to be closer to NMX. Based on this argument, we deduce that the MPI models (Figs. 2d,e) have weakly entraining convection, while NASA-GISS (Fig. 2c) and MRI-ESM2-0 (Fig. 2h) have strongly entraining convection. These patterns are also consistent with Ahmed and Neelin (2021a), who noted that the MPI models—in contrast to most CMIP6 models—are inadequately sensitive to LFT moisture. Figures 2a and 2b imply substantial entrainment rates for the observational baseline (but smaller than NASA-GISS and MRI-ESM2-0). If the difference between boundary layer θ_e and the LFT θ_{es} is taken as a measure of convective instability (Ahmed et al. 2020), it would appear that the MPI models are highly stable to convection when compared to NASA-GISS and MRI-ESM2-0. However, this measure is relevant for non-entraining convection—instead

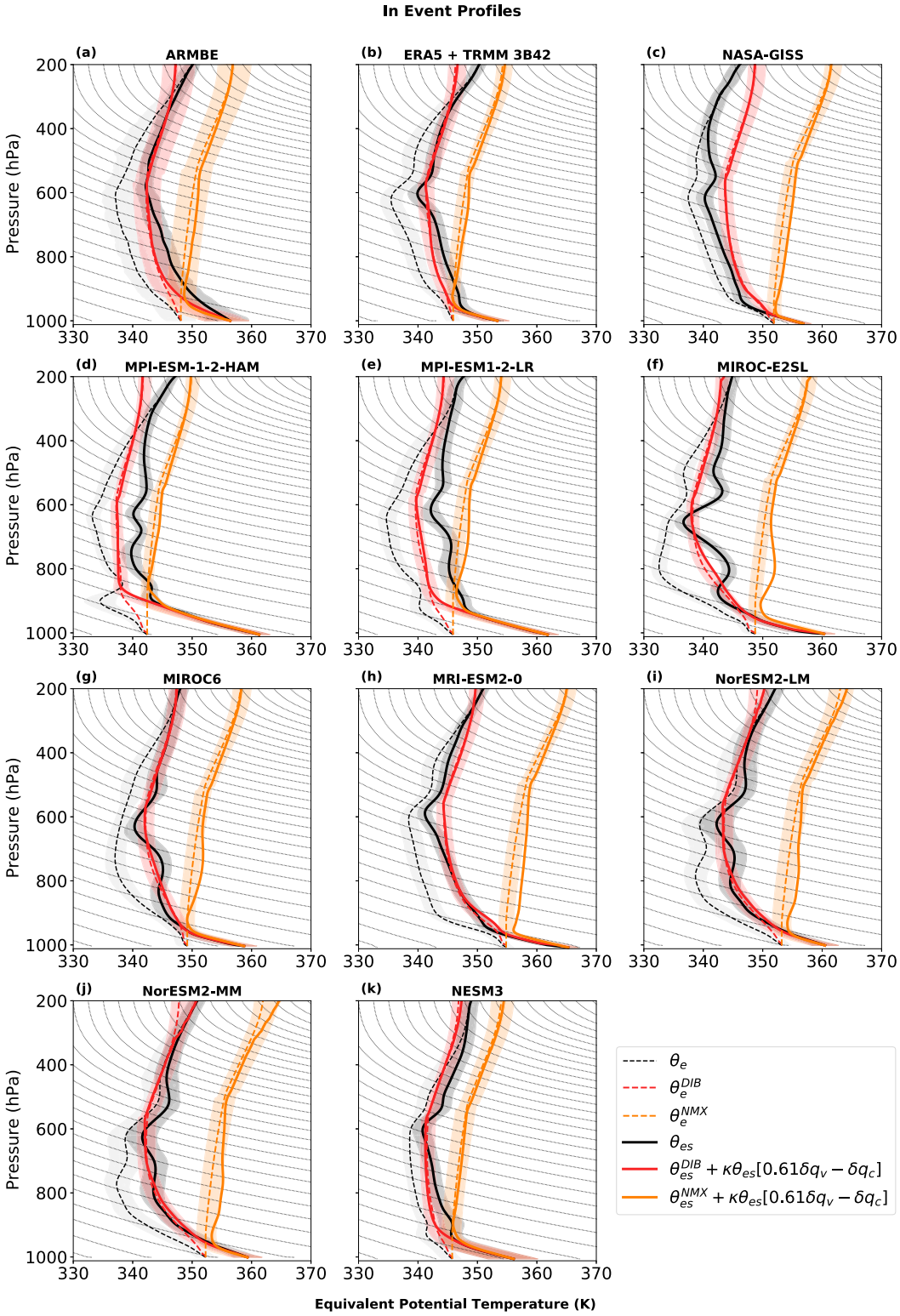

FIG. 2. Average profiles during raining times (precipitation rate $\geq$ 0.5 mm h^{-1}) for environmental θ_e (black dashed), θ_{es} (black solid), and plume trajectories, Deep-Inflow B (DIB; red) and nonmixing (NMX; orange). For the plume trajectories, solid lines show $\theta_{es} + \kappa\theta_{es}(0.61\delta q_v - \delta q_c)$ to evaluate buoyancy with condensate loading and water vapor effects included following (3), such that comparison to environmental θ_{es} is proportional to buoyancy, as in Fig. 1. Shading corresponds to 25th–75th percentiles. Contours are lines of constant potential temperature. Note that the nonmixing case θ_e profile is not constant in the vertical due to loss of condensate, since the x axis is reversible equivalent potential temperature.

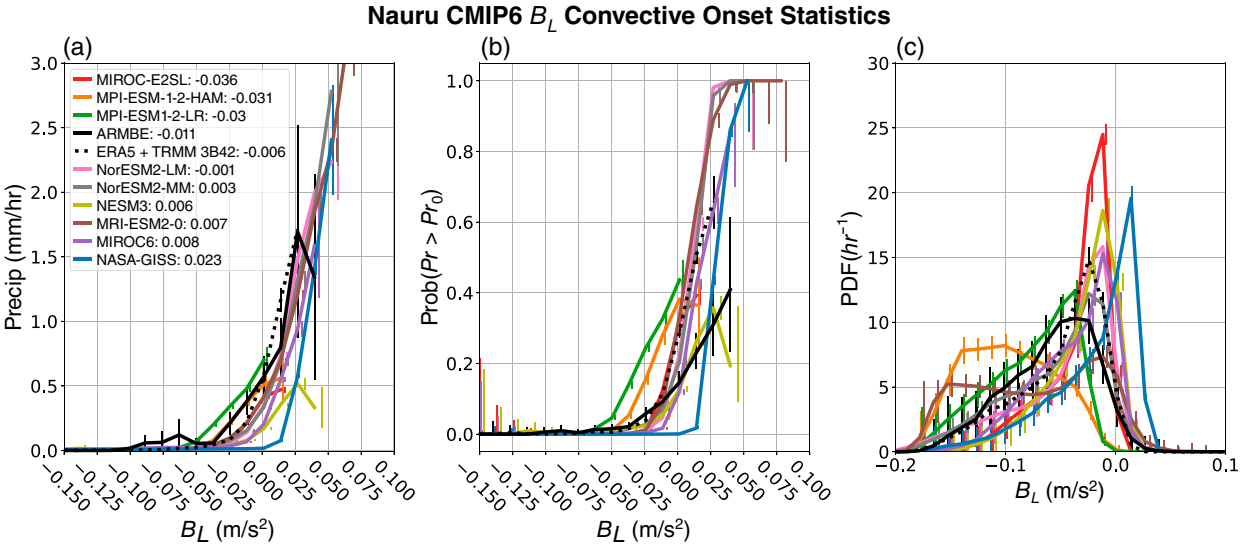

FIG. 3. The convective onset statistics for the observational and reanalysis products [black; ARMBE (solid) and ERA5 (dotted)] and the CMIP6 model cohort (colors) conditioned on a measure of lower tropospheric buoyancy B_L for the DIB-mixing plume model. (a) The conditional average precipitation with the legend in ascending order of a linear fit estimation of the critical B_L value of the pickup, error bars represent the standard error. (b) The conditional probability of precipitation (for precipitation rate ≥ 0.5 mm h^{-1}); error bars are the Wilson score interval for 95% confidence. (c) The PDFs of B_L, with 95% Wald interval error bars.

these results imply a trade-off between model entrainment and model θ_{es} profiles, previously noted in Singh and O'Gorman (2013) and Ahmed et al. (2020). This trade-off motivates construction of the pseudo-entrainment metric in section 7.

c. *Convective transition statistics stratified by lower tropospheric buoyancy B_L*

The convective transition statistics over tropical oceans for a number of CMIP6 models in B_L were presented in Ahmed and Neelin (2021a), including a baseline of ERA5 B_L matched with TRMM-3B42 precipitation. Similar statistics conditioned on column water vapor (CWV) and column relative humidity (CRH) for the models considered here were presented in Emmenegger et al. (2022), including ARMBE data as an additional measure of an observational baseline. Similar to the conditional-average precipitation rate $\langle P \rangle$ in CRH and CWV, the precipitation conditioned on B_L presented here in Fig. 3a, is sharp, or rapidly increases past some critical value of B_L—this rapid increase in $\langle P \rangle$ is referred to as the pickup. The critical value B_{Lc} is fit to each pickup as in Emmenegger et al. (2022), through finding the B_L value in which a linear fit of monotonically increasing $\langle P \rangle$ crosses 0.25 mm h^{-1}. The choice of 0.25 mm h^{-1} instead of 0 mm h^{-1} was chosen to exclude nonzero rates of precipitation at low B_L stemming from the persistent "model drizzle" problem, where models precipitate at low rates too often (Rushley et al. 2018; Stephens et al. 2010; Jing et al. 2017; Chen and Dai 2019) and other spurious deviations at low B_L (nonzero rates observed in the ARMBE data ~ -0.075 m s^{-2}). The B_{Lc} is listed in the legend of Fig. 3.

Results of the convective-onset statistics conditioned on B_L are similar to those reported in Emmenegger et al. (2022): most models pick up at slightly higher B_L than the baselines (the baselines are ARMBE and ERA5; Fig. 3a) and increase their probability of raining too quickly (Fig. 3c). In particular, the MPI models pick up early while NASA-GISS picks up noticeably late. Additionally, model pickups are driven primarily by an increasing probability of precipitation; that is, model precipitation rates in the raining state are not sufficiently sensitive to B_L.

It is important to note that differences are observed between the statistics of ERA5 and ARMBE. These arise from the same biases reported in Emmenegger et al. (2022)—ERA5 exhibits a cold bias in temperature with slightly lower humidity in the LFT, leading ERA5 to have a B_L PDF shifted toward higher values. The biases in ERA5 can be seen in the mean profiles of θ_{es} and θ_e (see Figs. 5l and 6l, respectively).

The PDFs of B_L (Fig. 3b) exhibit features similar to their counterparts in CRH and CWV [not shown; see Figs. 1–4 of Emmenegger et al. (2022)], in that the gradual slope of probability on left side of the PDF is limited by dry regime dynamics while sharp decrease in probability on right side of the PDF, or "drop-off," is limited by precipitation; that is, past the critical value of the pickup, precipitation becomes an effective moisture (hence B_L) sink. Ahmed et al. (2020) and Wolding et al. (2022) interpret the B_L PDFs from a QE perspective—convection relaxes a perturbed thermodynamic profile to an adjusted state—remarking that the peak of the PDF at B_{Lc} implies that B_{Lc} is the adjusted QE state. Excursions above B_{Lc} are consumed rapidly by convection while excursions below are consumed at a slower rate, as indicated by the slopes of the drop-off. More specifically—in the QE sense—the adjusted state represented by B_{Lc} represents a near-zero buoyancy state by which buoyancy generation via large-scale forcing is balanced by the convective consumption

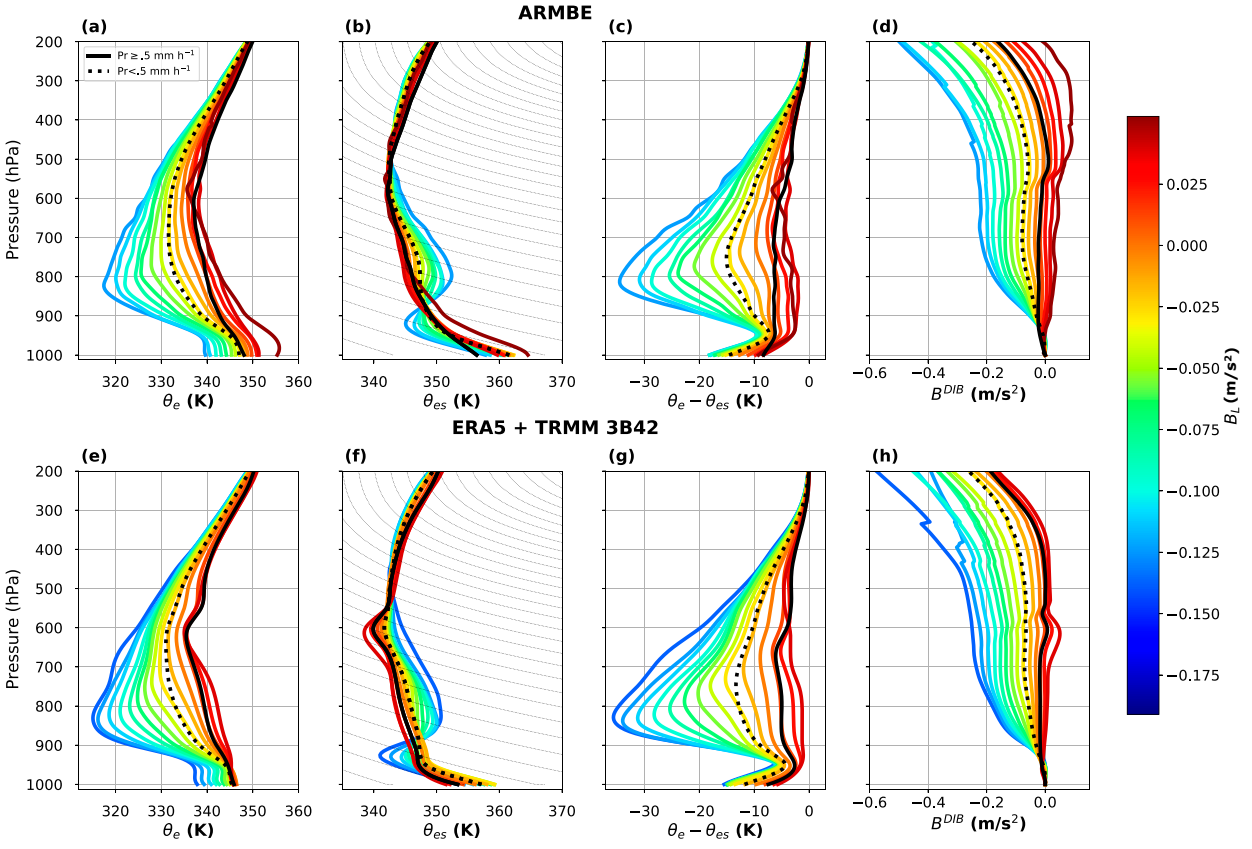

FIG. 4. Conditional-average profiles of (a),(e) θ_e on B_L, (b),(f) θ_{es}, (c),(g) subsaturation, and (d),(h) buoyancy for (top) ARMBE and (bottom) ERA5. Contours for θ_{es} are lines of constant potential temperature. The average over raining times (precipitation rate ≥ 0.5 mm h^{-1}) is represented by solid black lines; the average over nonraining times is represented by dotted black lines (precipitation rate < 0.5 mm h^{-1}).

of buoyancy (Arakawa 2004; Peters and Neelin 2006; Neelin et al. 2008; Ahmed et al. 2020; Wolding et al. 2022). Relationships between the QE state and adjustment process and convective instability as seen in vertical thermodynamic structures in observations and models are expanded on in sections 5d and 6. Building on Ahmed et al. (2020), we further explore the QE-state and its trade-offs between moisture and temperature induced by the variety of representations of entrainment in GCMs in section 7.

d. *Vertical profiles across the convective transition*

Figure 4 shows profiles conditioned on B_L for ERA5 and ARMBE. Figures 4a and 4e show the profiles of buoyancy B according to Eq. (1). The B_L binning is performed according to the average of these profiles from the surface to 600 hPa. Buoyancy remains close to zero through the boundary layer. At low (high) B_L, the B profiles decrease (stay relatively constant) throughout an intermediate layer from 900 to 700 hPa and flatten out until reaching the upper troposphere around 500 hPa. A kink in the profiles is apparent at high B_L bins due to contribution in temperature of freezing in the plume model.

Equivalent potential temperature θ_e increases throughout the column as B_L increases (Figs. 4a,e). At lower B_L bins, the θ_e profile decreases rapidly just above the boundary layer up to a minimum near the 850-hPa level before increasing up through the rest of the column. As B_L increases, θ_e begins to flatten out, the decrease of θ_e from the boundary layer lessens. The θ_e profile is more closely related to variations in the moisture content of the column as opposed to temperature (Ahmed and Neelin 2018). This can also be inferred from the θ_{es} structure (Figs. 4b,f), which is solely a measure of temperature in that higher B_L values are associated with a cooler column but exhibit a higher θ_e.

For both ARMBE and ERA5, higher buoyancy is achieved through a noticeable cooling and moistening in the LFT. At lower B_L, the θ_{es} (Figs. 4b,f) profile shows a decrease from the surface roughly along a line of constant potential temperature up until just below the 900-hPa level from where θ_{es} increases until reaching a maximum in the LFT at around the 800-hPa level in ARMBE and just below the 800-hPa level in ERA5, then gradually decreases with height. Higher B_L profiles continue to decrease their θ_{es} throughout the LFT, and are cooler through the LFT than lower B_L profiles. Both tendencies of moisture and temperature in increasing B_L contribute to large

differences in the subsaturation of the column in different B_L regimes as observed in Figs. 4c and 4g.

Higher B_L profiles associated with higher rates of conditionally averaged precipitation reflect parcels that are less diluted (less mixing) due to higher θ_e environments, as shown in Figs. 4a and 4e. The raining (solid; precipitation rate $\geq$ 0.50 mm h^{-1}) and nonraining cases (dashed) in Fig. 4 follow the trends of θ_e (Figs. 4a,e) and θ_{es} (Figs. 4b,f) noted above with increasing B_L—cooling and moistening of the LFT. In the case of precipitation in ARMBE, the boundary layer is cooler than the highest B_L bin and follows the trend of higher B_L through the rest of the column. The raining case in ERA5 does not display significant differences from the higher B_L bins across the environmental variables in Fig. 4.

The convective boundary layer lapse rate can be inferred from Fig. 4, where a parcel travels along a line of constant potential temperature up to its LCL; departures from a line of constant potential temperature are analogous to departures from a dry adiabatic lapse rate. In the ARMBE θ_{es} case (Fig. 4b) the binned profiles follow the trajectory of a dry adiabat (contours) through the boundary layer, regardless of their B_L value. Only in the raining case (solid black) does the boundary layer lapse rate deviate, starting from a cooler surface value with a shallower lapse rate than that predicted from a dry adiabat. The boundary layer follows a dry adiabat across all B_L and nonraining and raining regimes for ERA5 (Fig. 4f). Below the LCL, in the raining regime, the temperature is set by convective downdrafts associated with evaporative cooling. Just above the LCL, the temperature profiles for both ARMBE and ERA5 show an inversion at low-B_L bins. The inversion is eroded away as B_L transitions into higher values, and the lapse rate becomes steeper.

An additional note should be made on the virtual effect, and its contribution across different B_L regimes. With sufficiently unsaturated LFT, water vapor differences between the boundary layer and the LFT are large, leading to an increased virtual effect on buoyancy in low-B_L regimes. Vapor virtual effect contributions are found to be larger on average during nonraining times than raining times as the LFT is moister during raining times, permitting less dilution of ascending convective elements. Additionally, from Eq. (5), the buoyancy effects from the condensate in the plume model nearly cancels out the contribution from water vapor. In the case in which the condensate cap is set greater than 1 g kg^{-1}, the condensate contribution to buoyancy is greater than the vapor. Similar findings pointing to nonnegligible effects of condensate loading were explored in Xu and Randall (2001) and Bacmeister et al. (2012).

6. Intermodel differences in vertical thermodynamic structure

a. θ_e and θ_{es} vertical structures

Figure 5 displays the B_L-binned θ_{es} for the model cohort. With the exception of NASA-GISS, LFT θ_{es} decreases as B_L increases. A notable feature of Fig. 5 are the peaks in the vertical structures of θ_{es} of the models. The peaks of the MIROC models are described in Chikira and Sugiyama (2010) and attributed to thermodynamic variations associated with different cumulus convection regimes: 850, 650, and 350 hPa corresponding to three major regimes of cumulus convection—trade cumulus, cumulus congestus, and cumulonimbus. The peaks of the θ_{es} profiles of some models (especially MIROC-E2SL and MIROC6; Figs. 5f,g) in Fig. 5l—which lie close to the corresponding θ_e profile in Fig. 6l—could represent large-scale clouds in the domain as described by Chikira and Sugiyama (2010). Another complication these peaks introduce is biases in our calculation of B_L. These peaks are not visible in observations and reanalysis products, nor is it a robust feature across models.

The behavior of the NASA-GISS model's θ_{es} in transitioning from low to high B_L indicates the model as an outlier among the cohort—observations and the majority of models exhibit LFT cooling while NASA-GISS shows warming (Fig. 5c).

Figure 6 shows the θ_e profiles binned by B_L, similar to Fig. 5. Observations and models show a similar trend in increasing B_L with respect to moistening: a lower tropospheric minimum between 900 and 800 hPa that begins to flatten and shift toward higher θ_e as B_L increases. An inversion is observed in θ_{es} profiles in the layer just above the ABL in Figs. 4b and 4f. This inversion has been previously observed using dropsondes from the eastern Pacific in Raymond et al. (2003) and the authors note the inversion most likely arises from large-scale subsidence.

Spatial resolution considerations and their effect on the precipitation pickup for this model cohort were explored in Emmenegger et al. (2022) concluding that the convective transition statistics remain insensitive to spatial averaging. This insensitivity stems from the large spatial autocorrelation of moisture and temperature (Holloway and Neelin 2010; Abbott et al. 2016; Kuo et al. 2018).

b. Preconditioning of the convective environment

The trend in the θ_e profiles in Fig. 6 where the LFT moistens as B_L increases is possibly a result of detrainment from shallow cumulus. The deepening of cumulus congestus in the LFT and its detrainment of moisture preconditions the free troposphere for convection, as entrainment of moister air in a rising plume does not dilute buoyancy as much (Waite and Khouider 2010). Sensitivity tests in a cloud-resolving numerical experiment by Waite and Khouider (2010) found the moistening of the LFT to be the leading factor to the transition to deep convection, while the cooling of the troposphere and moistening of the ABL to be less important. An analysis by Hohenegger and Stevens (2013) found preconditioning by cumulus congestus to not be a dominant factor in the transition to deep cumulonimbus—the slow time scale of moistening by congestus is not consistent with the observed rapid transition to deep convection. Moreover, their results suggest moisture convergence to be the driving factor forced through mechanisms such as large-scale disturbances, waves, etc.

If the event is preceded by stratocumulus clouds, the cooling of the drizzle below the cloud base can lead to localized cooling and moistening below, destabilizing and moistening the subcloud layer, setting the environment to more favorable conditions for moist convection (Zuidema et al. 2017). In a scale analysis of contributions to plume buoyancy, Adames et al. (2021)

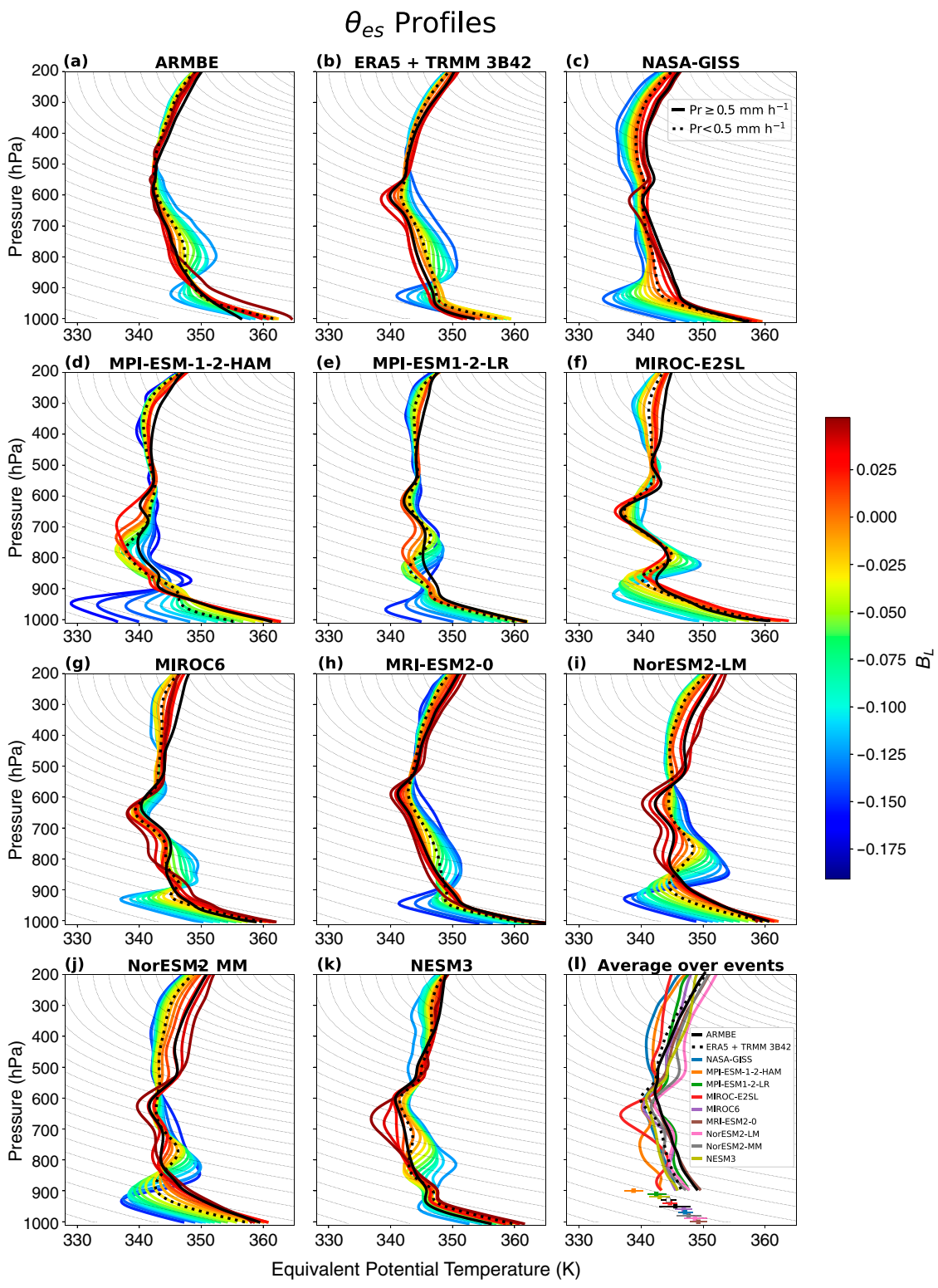

FIG. 5. (a)–(k) Binned profiles of θ_{es} according to B_L similar to Figs. 4b and 4f. The solid black line represents the average profile over raining times, while the dotted black line represents the average dry profile. (l) Average θ_{es} over raining events of the cohort (black solid lines in each panel) and the average θ_e of the boundary layer during raining events (dots) with 25th–75th confidence intervals.

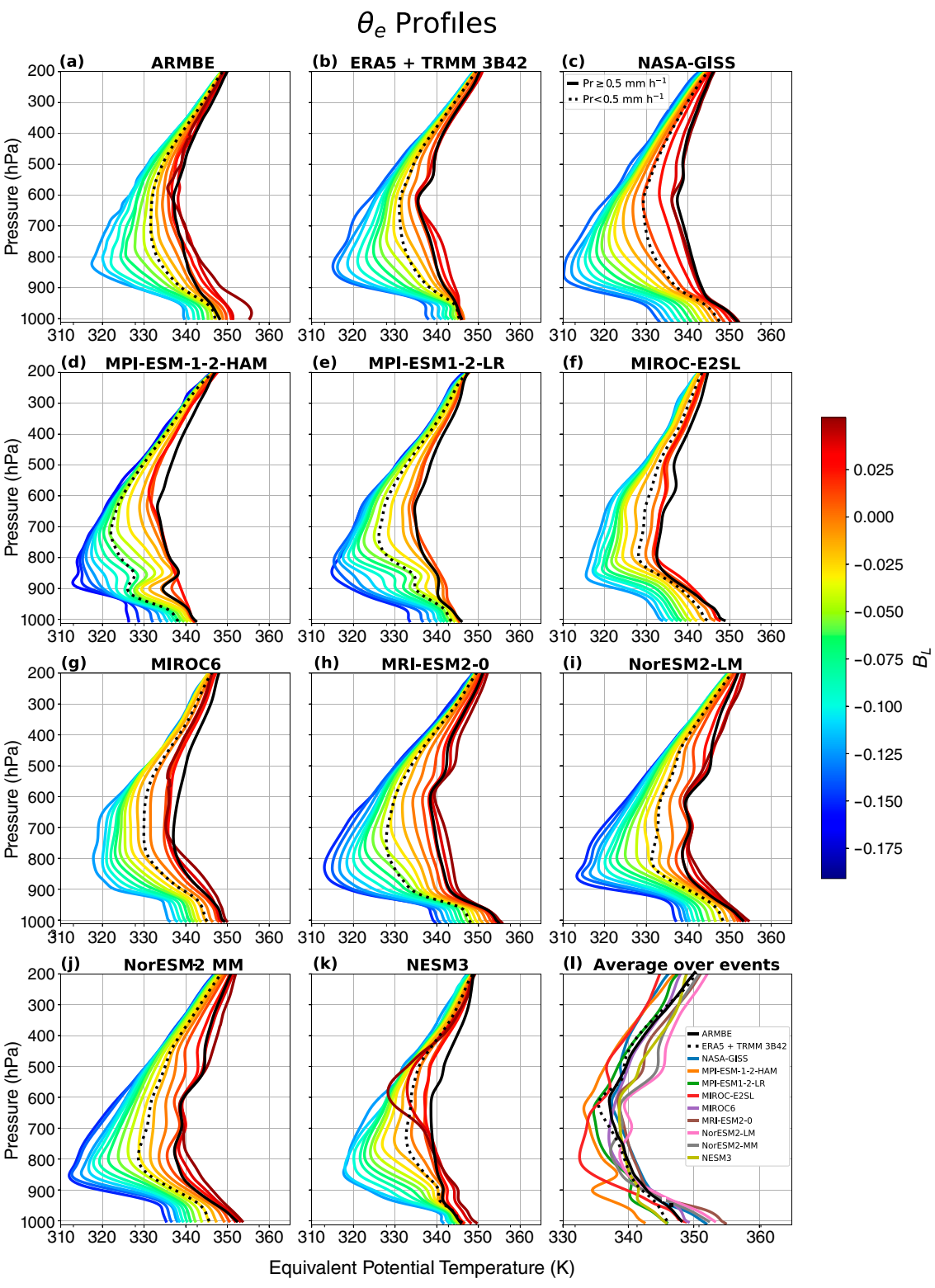

FIG. 6. As in Fig. 5, but for θ_e profiles.

found the largest source to be adiabatic moistening and cooling in the LFT.

Subsaturation, $\theta_e - \theta_{es}$, is perhaps the most important factor in the trajectory of a mixing plume, particularly the subsaturation of the LFT. This measure represents the additional moist entropy needed to bring the environment to saturation and determines the dilution of the rising plume (Ahmed and Neelin 2018). The convective transition statistics compiled in subsaturation are displayed in Fig. S1. The conditional-average precipitation rate also exhibits a sharp pickup when conditioned on subsaturation of the environment (Fig. S1). This illustrates the importance of this component of B_L, capturing the effect of entraining relatively moist versus relatively dry LFT air. Note that the subsaturation of the LFT takes two preconditioning effects (Zhang and Klein 2010) into account—in addition to moisture, the variations in temperature measured by θ_{es} can contribute.

Adames et al. (2021) found the fast time scale on which the cooling and moistening of the LFT occurs is consistent with inertio-gravity waves. With this in mind, a sufficiently moist column may be driven to saturation and convection. As noted in Raymond (1995), a marginally subsaturated column within a few kelvins to zero are convective, as a transient gravity wave can lower the θ_{es} of the environment. Another large contribution to buoyancy generation and destabilization is vertical advection of moisture. Convection moistens the LFT if moistening from updraft detrainment exceeds drying from downdraft detrainment (Adames et al. 2021).

7. The pseudo-entrainment diagnostic

Examination of observed and model θ_e and θ_{es} profiles in Fig. 2 suggested a decrease in θ_{es} through the lower free troposphere that is likely associated with entrainment interacting with the lower free tropospheric humidity. We now construct a pseudo-entrainment metric, in which bulk entrainment is estimated using θ_e and θ_{es} profiles.

a. Derivation

Assuming that the plume entrains environmental air from some combination of levels below, or that there exists some influence function (Ahmed and Neelin 2018; Schiro et al. 2018), the relationship of the estimated updraft θ_e has the form

$$\theta_e^p = \int_p^{p_s} I(p, p')\theta_e(p')dp', \tag{6}$$

where

$$I(p, p') = \frac{1}{M(p)}\frac{dM(p')}{dp'}$$

is the influence function with M is the upward mass flux. Differentiating (6) with respect to p gives the simple plume equation

$$\frac{d\theta_e^p}{dp} = \epsilon(\theta_e - \theta_e^p), \tag{7}$$

where

$$\epsilon = \frac{1}{M(p)}\frac{dM(p)}{dp} = I(p, p)$$

is the entrainment coefficient and detrainment is neglected.

To a first approximation using the zero buoyancy assumption (Singh and O'Gorman 2013) and taking $\theta_{es} = \theta_e^p$ in (7) gives

$$\frac{d\theta_e^p}{dp} = \epsilon(\theta_e - \theta_{es}). \tag{8}$$

The right-hand side of (8) is the environmental subsaturation, a measure of environmental dryness. Assuming now that the entrainment is constant through the LFT and integrating (8) from the top of the boundary layer (900 hPa) to 600 hPa gives

$$\epsilon \approx \tilde{\epsilon} = \frac{\theta_{es}^{600} - \theta_e^{\mathrm{BL}}}{\langle \theta_e^- \rangle}, \tag{9}$$

where $\tilde{\epsilon}$ is termed the pseudo-entrainment, a bulk measure of entrainment in the LFT, and $\langle \theta_e^- \rangle$ is the vertically integrated subsaturation from 900 to 600 hPa. In deriving (9), we have assumed that the plume leaves the boundary layer with the average θ_e of the boundary layer, θ_e^{BL}. At 600 hPa, the plume θ_e is assumed equal to the environmental saturated θ_e ($=\theta_{es}^{600}$). The upper limit of the integral in (9) is restricted to 600 hPa for the following reasons: (i) the plume properties below the freezing layer are found to have the strongest relationship to precipitation (Holloway and Neelin 2009; Schiro et al. 2018; Ahmed and Neelin 2021b) and (ii) 600 hPa lies below the tropical freezing layer, so ice transformation effects can be neglected when formulating (9). The pseudo-entrainment diagnostic is a function of the environmental stability [the numerator in (9)] and subsaturation [the denominator in (9)].

A similar derivation for a zero-buoyancy entraining plume model was used in Singh and O'Gorman (2013); in their model, the entrainment rate is prescribed as the $\epsilon(z) = \hat{\epsilon}/z$ case (the same scheme used in our Deep-Inflow B calculations) where $\hat{\epsilon}$ is a constant. Deep-Inflow B considerations can be applied to Eq. (9), by substituting $\epsilon = \hat{\epsilon}(p - p_0)^{-1}$ which applies weighting to the isobaric layers of integrated subsaturation profile over the entraining layer. The main results remain unchanged. For simplicity, we stick to our formulation in (9).

We wish to emphasize that pseudo-entrainment and entrainment in a model convective scheme are not interchangeable. First, the pseudo-entrainment similarity to entrainment in (8) applies in the limit of small buoyancy, which is often violated at short time scales, hence the choice to diagnose the pseudo-entrainment from the average conditions over raining events. Second, models often produce some deep convection at the grid scale (e.g., Norris et al. 2021). The pseudo-entrainment includes effects of such events, for which entrainment is by the flow into the grid cell from neighboring nonconvecting grid cells, as elaborated below. Overall, the large-scale pseudo-entrainment measure aims to capture the aggregate effect of an

ensemble of convective entities originating at any level in the LFT (below 600 hPa), not the entrainment rate that would apply during a particular convective event or in a specific parameterization. In the following section, we will be applying the pseudo-entrainment estimation to the environmental profiles at the Nauru site.

b. *Model diagnosis*

The pseudo-entrainment diagnostic is now applied to constrain climate model entrainment-stability tradeoffs. For this we use nine CMIP6 models along with six CAM5 parameter perturbation runs. Note that (9) is only applicable during convecting times since it is derived from an entraining plume equation (6). We therefore estimate all the environmental θ_e-based variables (θ_e^{BL}, θ_{es}^{600}, and $\langle\theta_e^-\rangle$) as averages during times in which the precipitation rate exceeds 0.5 mm h^{-1}. Figure 7 shows θ_e^{BL} and the θ_{es}^{600} of each model computed this way, along with comparisons to ARMBE and ERA5 data. Confidence ellipses are computed from 1000 bootstrap realizations of the average raining profile (sampled with replacement from the raining events in each dataset), using the covariance matrix to fit an ellipse that would contain 95% of the samples if the distribution were Gaussian. For models and ERA5, the ellipses are smaller than the symbols due to large number of soundings, but may be seen for ARMBE and the CAM5 runs due to smaller sample size. A related measure for regional representativeness is discussed below.

Under QE assumptions, the instability measure, $\theta_e^{\mathrm{BL}} - \theta_{es}^{600}$, may be regarded as a "plume lapse rate" relative to that of a nonentraining parcel through the LFT if $\theta_e^{\mathrm{BL}} \sim \theta_{es}$ at the top of the boundary layer (i.e., the level of free convection is near 900 hPa). We use this term for brevity, noting that it would be zero for an environmental profile neutral to nonentraining, reversible plumes. The DIB plume in Fig. 2 (θ_e^{DIB}; red curve) is approximated by the average of levels below; its θ_e at the top of the boundary layer (900 hPa) is equivalent to the θ_e^{BL} value displayed in Fig. 7. At the top of the boundary layer, the DIB plume lies close to its environmental θ_{es} for NASA-GISS, the MIROC models, MRI-ESM2-0, and the NorESM2 models (comparison of red to solid black curves in Figs. 2c,f–j). ARMBE, ERA5, the MPI models, and NESM3 environmental θ_{es} are more similar to the NMX plume at the top of the boundary layer (comparison of orange to black curve in Figs. 2a,b,d,e,k). The estimation of the boundary layer θ_e depends on boundary layer mixing assumptions, which may be different among model convective schemes (and varying in observations). Surface boundary layer values for those models which appear to experience less mixing out of the boundary are included in Fig. 7 (open circles) for reference.

As an indicator of how well values at Nauru represent the region, we also include an ellipse, similar to a 95% confidence ellipse, for the for the ERA5 western Pacific (5°S–5°N, 100°E–180°) averaged profiles over raining times in 2006. This ellipse is fit such that it contains 95% of the samples from the distribution over this region. In addition to sampling error (relatively small) it includes variations due to point to point differences within the region. For the ERA5 western Pacific,

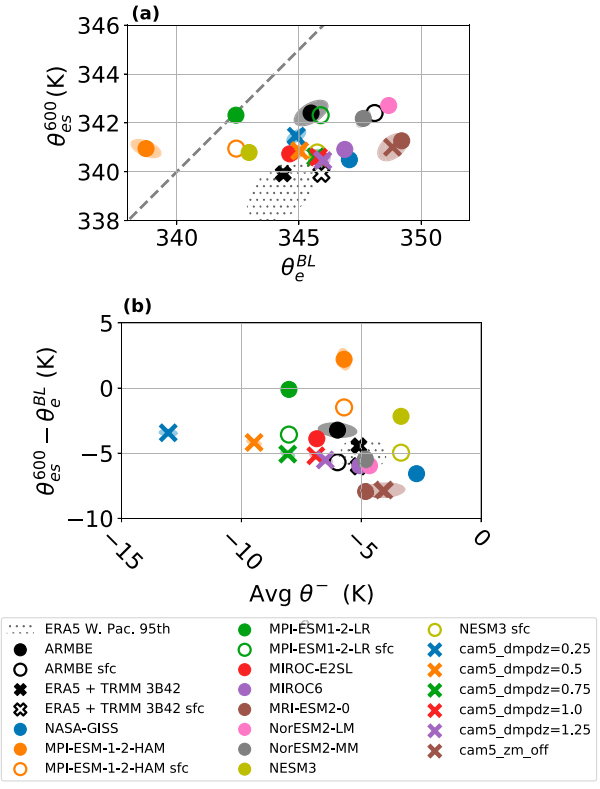

FIG. 7. (a) Average atmospheric boundary layer (ABL; defined as 1000–900 hPa; closed markers) with surface θ_e values (open markers) plotted against the θ_{es} at the 600-hPa level of the average raining profiles, with the one-to-one line plotted as a reference (gray dashed) and (b) the average LFT subsaturation (900–600 hPa) during raining times plotted against the theoretical plume lapse rate [$\theta_{es}^{600} - \theta_e^{\mathrm{BL}}$; subtracting the two quantities plotted in (a)] of the average raining profile. Quantities are calculated from the profiles displayed in Fig. 2. Shaded regions are 95% confidence ellipses (in most cases these are smaller than the marker) which contain 95% of the samples from the underlying Gaussian distribution. The dotted region indicates the western Pacific regional spread in ERA5 (see text). CAM5 perturbed-physics experiments are included with varying entrainment rates (dmpdz) of 0.25, 0.50, 0.75, 1.0 (control), and 1.25 km^{-1}, and a case where the subgrid convective parameterization is turned off (zm_off) as colored x markers.

this ellipse is elongated in a direction corresponding to constant lapse rate, i.e., θ_e^{BL} increases are aligned with θ_{es}^{600} increases, parallel to the one-to-one line in Fig. 7.

Models which use the Tiedtke-type convective parameterization—which use moisture convergence in the convective trigger—the MPI models and NESM3, are more stable than observations, while other models in the cohort—the majority of which use a CAPE-based triggers and closures—look to exhibit less stability (convective parameterization assumptions are listed in Table 1).

The total dilution of the bulk plume is characterized by $\theta_e^{\mathrm{BL}} - \theta_{es}^{600}$, often discussed as an instability measure since positive values would yield convective instability for nonentraining plume—noting that here the interpretation is as a profile

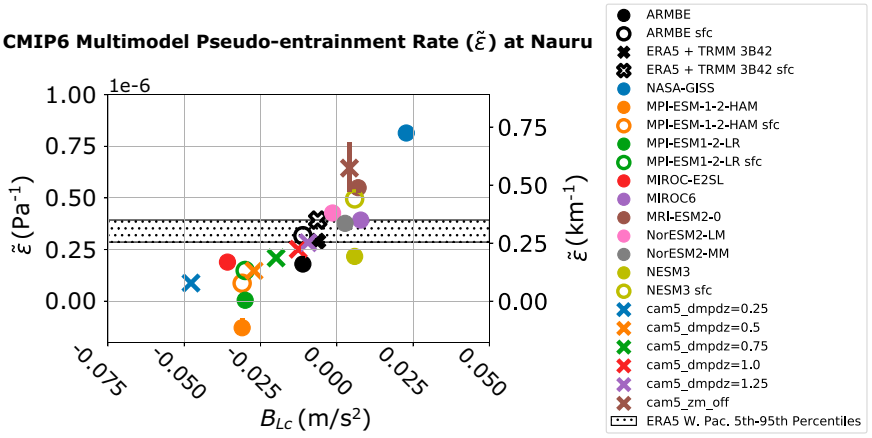

FIG. 8. The pseudo-entrainment rate $\tilde{\epsilon}$ plotted against the critical value of the B_L pickup. Vertical bars show the 5th–95th confidence interval, but are only visible for CAM-ZM-OFF. The dotted area shows 5th–95th range from the western Pacific, similar to Fig. 7, i.e., a measure of regional variations in the pseudo-entrainment.

that is typically only marginally unstable to entraining plumes. This measure is similar to the deep convective inhibition quantity introduced in Raymond et al. (2003) where the authors showed a correlation between larger differences between boundary layer moist entropy and an intermediate layer (810–830 hPa) and deep convection.

The environmental subsaturation in the intermediate layer plays a defining role and acts with entrainment in determining the degree to which the bulk plume is diluted in its ascent. Consider the scenario where the entrainment among a model cohort is fixed. In our formulation, if the stability differs, the conclusion is that the subsaturation of the environments differ—larger (smaller) lapse rates are the result of a more (less) subsaturated environment due to the incorporation of drier (moister) air into the plume. Figure 7b shows the average subsaturation of the intermediate layer (900–600 hPa) to the lapse rate of the environment. The subsaturation–instability relationship of the model cohort is much more complicated than this as observed in Fig. 7b; models exhibit varying degrees of subsaturation and lapse rates. We can tie these two environmental factors together and derive a single quantitative diagnostic, the pseudo-entrainment diagnostic, as an estimator of the bulk entrainment rate. The pseudo-entrainment diagnostic is, more succinctly, the ratio of the instability to the subsaturation of a raining column.

The pseudo-entrainment formulation illustrates the trade-off between the subsaturation and the lapse rate; in order for a model with a high (low) bias prescribed entrainment to replicate the observed lapse rate, it must compensate with higher (lower) subsaturation. This trade-off has been explored in previous studies: (Mapes and Neale 2011; Kim et al. 2013, 2012; Ahmed et al. 2020), increasing entrainment increases the influence of the ambient subsaturation at the expense of the LFT stratification. Buoyancy-based cumulus parameterizations (those with considerations of CAPE or cloud-work) adjust precipitating environments to near-zero buoyancy measures; the quasi-equilibrium (QE) state in models with low entrainment is characterized by neutral lapse rates while the QE state of models with high-entrainment is LFT saturation (Ahmed et al. 2020).

We calculate $\tilde{\epsilon}$ with the average profile over raining times for each model. Figure 8 shows the results of the pseudo-entrainment rate, plotted against the critical value of the precipitation pickup B_{Lc}, the B_L value where the precipitation pickup begins to increase rapidly.

A near linear relationship is observed between B_{Lc} and $\tilde{\epsilon}$, models with a higher pseudo-entrainment tend to exhibit a pickup at higher B_L. The pseudo-entrainment estimation is able to discern between those environments resulting from an increasing entrainment parameter within a convective scheme; increasing the entrainment rate in the CAM5 model leads to a higher $\tilde{\epsilon}$ and a higher B_L pickup (colored x markers in Fig. 8). As a model entrainment parameter is decreased, the threshold for the convective trigger (such as CAPE) is met in drier environments, and models with lower entrainment have drier and warmer columns during convection. We underline that the pseudo-entrainment estimator is for an overall effect of entrainment. This could include contributions from more than one entrainment scheme if present; more importantly, when grid-scale convection occurs in the model, which is not infrequent, the overall entrainment includes grid-scale inflow with neighboring cells serving as the environment. This may be seen with the ZM-OFF experiment, for which deep convection happens entirely at the grid scale and which thus has a high pseudo-entrainment.

The pseudo-entrainment diagnostic, being a function of temperature lapse rate and subsaturation, presents a constraint on model behavior if entrainment is not correctly represented. For instance, if a model's convective scheme entrains too heavily, the bulk plume dilutes quickly, and this is reflected in the environmental θ_{es} as a steeper lapse rate and a higher measure of instability. In this high (low) entrainment case, to counter the production of large and too unstable (small and too stable) lapse rates, the bulk plume would need

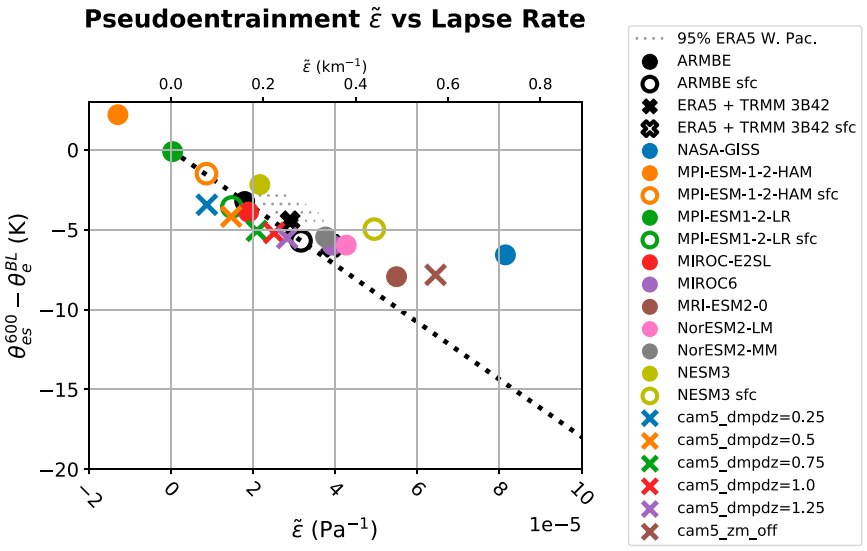

FIG. 9. The pseudo-entrainment $\tilde{\epsilon}$ plotted against the theoretical plume lapse rate (calculated from the average profiles during raining times). The reference line refers to the ARMBE LFT subsaturation; models which lie to the right (left) of this line have a moist (dry) bias for their given lapse rate. The dotted region shows western Pacific regional variations in ERA5 as in Figs. 7 and 8.

to mix with less (more) subsaturated air, or the column would need to moisten to a sufficient degree.

Model moisture biases are often framed with the consideration of the convective trigger (e.g., models with lower entrainment may reach their threshold for convection in drier environments; Ahmed and Neelin 2021a). The components of the pseudo-entrainment diagnostic—the instability and subsaturation—provide another, perhaps more consequential, view of how entrainment biases affect environmental behavior during convective events. Models with pseudo-entrainment rates that are too large must produce a higher moisture bias to accurately represent the stability of the environment.

This is shown in Fig. 9, which displays the pseudo-entrainment against the instability of the observations and model cohort. The reference line (black-dotted) shows the values of pseudo-entrainment and the instability needed to replicate the subsaturation of the ARMBE data—higher $\tilde{\epsilon}$ implies a higher stability if the subsaturation is constant. Models that lie to the right (left) of the reference line have a high (low) moisture bias. Most notably in Fig. 9, the NASA-GISS model must have a high moisture bias, given that its pseudo-entrainment is so large. A major implication of Fig. 9 is that if NASA-GISS moisture were not compensating for its high $\tilde{\epsilon}$, its instability would be too large compared to observations (−15 K).

8. Conclusions

A simple plume model based on the conservation of equivalent potential temperature θ_e allows for estimations of instability similar to measures of CAPE from snapshots of vertical thermodynamic structures. The θ_e definition of buoyancy provides a favorable framework for tropical climatologies that are shaped by moist convection driven by the onset of conditional instability. The presence of a rapid increase in precipitation conditioned on heavily entraining plume buoyancy $\langle P \rangle$ across the cohort of CMIP6 models indicates a high degree of correlation between heavy lower-free tropospheric (LFT) mixing and the onset of convection in model convective schemes. Binning the thermodynamic environments by a theoretical value of LFT buoyancy B_L shows the environment generates buoyancy through the combination of LFT cooling and moistening. Most models qualitatively capture this cooling and moistening behavior, the exception being the NASA-GISS model which warms in addition to moistening. Contrary to previous work which points to insufficient sensitivity of the prior (CMIP5) generation of GCMs to LFT moisture (Rushley et al. 2018), the proximity of the critical values of $\langle P \rangle$ between CMIP6 models and observations suggests the majority of CMIP6 models perform fairly well in their sensitivity to environmental moisture through the mixing process.

Emmenegger et al. (2022) showed that a cohort of CMIP6 models perform relatively well in replicating the statistics of column-integrated measures such as column relative humidity (CRH) and column water vapor and precipitation. The analysis presented here dissects the vertical thermodynamic structures of the model cohort, concluding that models perform well with respect to CRH but at the expense of their climatological stability due to the constraint presented by inaccurate representation of the entrainment process. A few models in this cohort, NASA-GISS and MRI-ESM2-0, are shown to exhibit environments consistent with too much entrainment in their convective schemes and must compensate with a wetter column during convection in order to keep their column at a realistic level of stability (as determined by the difference between θ_{es} of the LFT and θ_e of the boundary layer).

These conclusions are reached through the derivation of the pseudo-entrainment diagnostic, an estimation of an entrainment rate undergone by a bulk plume between the boundary layer and the freezing level. The pseudo-entrainment is the ratio of the bulk plume lapse rate (the expected change a parcel undergoes in its ascent, estimated by difference of the freezing level θ_{es} and boundary layer θ_e) and the integrated subsaturation (the expected properties of the air the parcel mixes with) of the average raining environment. It is shown in Fig. 8 that the pseudo-entrainment serves as a reasonable indicator of the critical value of the pickup, with a higher pseudo-entrainment diagnostic predicting pickup at a higher B_L value. These results are consistent with our postulate that larger measures of apparent convective instability on average during raining events are a consequence of too heavy entrainment. In section 7, the consequences of the incorrect treatment of the entrainment process in the climatological structures of humidity and instability are assessed. Figure 9 displays the constraint in which CWV and CRH statistics may be accurately represented by models with incorrect entrainment, but only so at the expense of climatological instability—models with higher (lower) entrainment must accommodate with higher (lower) climatological instability to accurately represent environmental moisture. In the case that entrainment is too high, models must sufficiently saturate to keep climatological instability at some reasonable range to that of observations. Such is the case for the NASA-GISS model; it shows a significantly higher measure of pseudo-entrainment, and to keep its stability within a reasonable range of observations, it compensates with higher climatological moisture. The pseudo-entrainment diagnostic shows models that use variants of the Tiedtke convective scheme and low entrainment runs of CAM5 display environments consistent with small entrainment, with small plume lapse rates and larger subsaturation that lead to early pickups in B_L. Furthermore, some models that behave reasonably in terms of bulk entrainment effects exhibit variations in vertical structure even for averages over raining events that do not correspond to observations. We postulate that the factors of the pseudo-entrainment diagnostic analyzed here likely shape features of CMIP6 warming scenario experiments, given the delicate balance between lapse rate (instability) and water vapor (subsaturation) feedbacks, which shape the structure of warming (Bao et al. 2021).

Acknowledgments. This work was supported under National Science Foundation AGS-1936810, National Oceanic and Atmospheric Administration NA21OAR4310280 (TE, FA, YHK and JDN), by Department of Energy DE-SC0022995 (TE, FA and JDN), and National Aeronautics and Space Administration grant 80NM0018F0617 (TE). YHK was also supported under NA18OAR4320123 from the National Oceanic and Atmospheric Administration, U.S. Department of Commerce. The statements, findings, conclusions, and recommendations are those of the author(s) and do not necessarily reflect the views of the National Oceanic and Atmospheric Administration, or the U.S. Department of Commerce. This work was also partially supported by the U.S. Department of Energy's Atmospheric Radiation Measurement program (ARM). Work at LLNL was performed under the auspices of the U.S. DOE by Lawrence Livermore National Laboratory under Contract DE-AC52-07NA27344.We acknowledge the U.S. Department of Energy's ARM program and the Program for Climate Model Diagnosis and Intercomparison to Earth System Science Portals for making CMIP data available.

Data availability statement. ARM data are openly available through the U.S. Department of Energy's Atmospheric Radiation Measurement Portal for ARM (https://doi.org/10.5439/1027369, cited in Gaustad and Riihimaki 1998) and ARMBE (https://doi.org/10.5439/1333228, cited in Xie et al. 2010). ERA5 data are available through the Climate Data Store portal (https://doi.org/10.24381/cds.bd0915c6, as cited in Hersbach et al. 2020). TRMM-3b42 data are available through NASA's Earth Data portal (https://doi.org/10.5067/TRMM/TMPA/3H/7, as cited in Tropical Rainfall Measuring Mission 2011). All model data are available through the Climate Model Diagnosis and Intercomparison to Earth Systems Science Portal at https://aims2.llnl.gov/search.

REFERENCES

Abbott, T. H., S. N. Stechmann, and J. D. Neelin, 2016: Long temporal autocorrelations in tropical precipitation data and spike train prototypes. *Geophys. Res. Lett.*, **43**, 11 472–11 480, https://doi.org/10.1002/2016GL071282.

Adames, Á. F., S. W. Powell, F. Ahmed, V. C. Mayta, and J. D. Neelin, 2021: Tropical precipitation evolution in a buoyancy-budget framework. *J. Atmos. Sci.*, **78**, 509–528, https://doi.org/10.1175/JAS-D-20-0074.1.

Ahmed, F., and C. Schumacher, 2015: Convective and stratiform components of the precipitation-moisture relationship. *Geophys. Res. Lett.*, **42**, 10 453–10 462, https://doi.org/10.1002/2015GL066957.

——, and ——, 2017: Geographical differences in the tropical precipitation-moisture relationship and rain intensity onset. *Geophys. Res. Lett.*, **44**, 1114–1122, https://doi.org/10.1002/2016GL071980.

——, and J. D. Neelin, 2018: Reverse engineering the tropical precipitation–buoyancy relationship. *J. Atmos. Sci.*, **75**, 1587–1608, https://doi.org/10.1175/JAS-D-17-0333.1.

——, and ——, 2021a: A process-oriented diagnostic to assess precipitation-thermodynamic relations and application to CMIP6 models. *Geophys. Res. Lett.*, **48**, e2021GL094108, https://doi.org/10.1029/2021GL094108.

——, and ——, 2021b: Protected convection as a metric of dry air influence on precipitation. *J. Climate*, **34**, 3821–3838, https://doi.org/10.1175/JCLI-D-20-0384.1.

——, Á. F. Adames, and J. D. Neelin, 2020: Deep convective adjustment of temperature and moisture. *J. Atmos. Sci.*, **77**, 2163–2186, https://doi.org/10.1175/JAS-D-19-0227.1.

Allen, M. R., and W. J. Ingram, 2002: Constraints on future changes in climate and the hydrologic cycle. *Nature*, **419**, 224–232, https://doi.org/10.1038/nature01092.

Ando, T., and Coauthors, 2021: Description of MIROC6 AGCM. CCSR Rep. 65, 137 pp., https://ccsr.aori.u-tokyo.ac.jp/ccsrlist/Description_of_MIROC6_AGCM.pdf.

Arakawa, A., 2004: The cumulus parameterization problem: Past, present, and future. *J. Climate*, **17**, 2493–2525, https://doi.org/10.1175/1520-0442(2004)017<2493:RATCPP>2.0.CO;2.

——, and W. H. Schubert, 1974: Interaction of a cumulus cloud ensemble with the large-scale environment, Part I. *J. Atmos. Sci.*, **31**, 674–701, https://doi.org/10.1175/1520-0469(1974)031<0674:IOACCE>2.0.CO;2.

Bacmeister, J. T., P. H. Lauritzen, A. Dai, and J. E. Truesdale, 2012: Assessing possible dynamical effects of condensate in high resolution climate simulations. *Geophys. Res. Lett.*, **39**, L04806, https://doi.org/10.1029/2011GL050533.

Bao, J., and B. Stevens, 2021: The elements of the thermodynamic structure of the tropical atmosphere. *J. Meteor. Soc. Japan*, **99**, 1483–1499, https://doi.org/10.2151/jmsj.2021-072.

——, ——, L. Kluft, and D. Jiménez-de-la Cuesta, 2021: Changes in the tropical lapse rate due to entrainment and their impact on climate sensitivity. *Geophys. Res. Lett.*, **48**, e2021GL094969, https://doi.org/10.1029/2021GL094969.

Bechtold, P., M. Köhler, T. Jung, F. Doblas-Reyes, M. Leutbecher, M. J. Rodwell, F. Vitart, and G. Balsamo, 2008: Advances in simulating atmospheric variability with the ECMWF model: From synoptic to decadal time-scales. *Quart. J. Roy. Meteor. Soc.*, **134**, 1337–1351, https://doi.org/10.1002/qj.289.

Bentsen, M., and Coauthors, 2019: NCC NorESM2-MM model output prepared for CMIP6 CMIP historical. Earth System Grid Federation, accessed 22 May 2020, https://doi.org/10.22033/ESGF/CMIP6.8040.

Betts, A. K., 1986: A new convective adjustment scheme. Part I: Observational and theoretical basis. *Quart. J. Roy. Meteor. Soc.*, **112**, 677–691, https://doi.org/10.1002/qj.49711247307.

——, and M. J. Miller, 1986: A new convective adjustment scheme. Part II: Single column tests using GATE wave, BOMEX, ATEX and Arctic air-mass data sets. *Quart. J. Roy. Meteor. Soc.*, **112**, 693–709, https://doi.org/10.1002/qj.49711247308.

Bretherton, C. S., and P. K. Smolarkiewicz, 1989: Gravity waves compensating subsidence and detrainment around cumulus clouds. *J. Atmos. Sci.*, **46**, 740–759, https://doi.org/10.1175/1520-0469(1989)046<0740:GWCSAD>2.0.CO;2.

——, M. E. Peters, and L. Back, 2004: Relationships between water vapor path and precipitation over the tropical oceans. *J. Climate*, **17**, 1517–1528, https://doi.org/10.1175/1520-0442(2004)017<1517:RBWVPA>2.0.CO;2.

Cao, J., and B. Wang, 2019: NUIST NESMv3 model output prepared for CMIP6 CMIP historical. Earth System Grid Federation, accessed 22 May 2020, https://doi.org/10.22033/ESGF/CMIP6.8769.

——, and Coauthors, 2018: The NUIST Earth System Model (NESM) version 3: Description and preliminary evaluation. *Geosci. Model Dev.*, **11**, 2975–2993, https://doi.org/10.5194/gmd-11-2975-2018.

Chen, D., and A. Dai, 2019: Precipitation characteristics in the Community Atmosphere Model and their dependence on model physics and resolution. *J. Adv. Model. Earth Syst.*, **11**, 2352–2374, https://doi.org/10.1029/2018MS001536.

Chikira, M., and M. Sugiyama, 2010: A cumulus parameterization with state-dependent entrainment rate. Part I: Description and sensitivity to temperature and humidity profiles. *J. Atmos. Sci.*, **67**, 2171–2193, https://doi.org/10.1175/2010JAS3316.1.

Covey, C., P. J. Gleckler, C. Doutriaux, D. N. Williams, A. Dai, J. Fasullo, K. Trenberth, and A. Berg, 2016: Metrics for the diurnal cycle of precipitation: Toward routine benchmarks for climate models. *J. Climate*, **29**, 4461–4471, https://doi.org/10.1175/JCLI-D-15-0664.1.

Del Genio, A. D., 2012: Representing the sensitivity of convective cloud systems to tropospheric humidity in general circulation models. *Surv. Geophys.*, **33**, 637–656, https://doi.org/10.1007/s10712-011-9148-9.

——, and M.-S. Yao, 1993: Efficient cumulus parameterization for long-term climate studies: The GISS scheme. *The Representation of Cumulus Convection in Numerical Models*, Springer, 181–184.

——, and J. Wu, 2010: The role of entrainment in the diurnal cycle of continental convection. *J. Climate*, **23**, 2722–2738, https://doi.org/10.1175/2009JCLI3340.1.

Emanuel, K. A., 1994: *Atmospheric Convection*. Oxford University Press, 580 pp.

——, J. D. Neelin, and C. S. Bretherton, 1994: On large-scale circulations in convecting atmospheres. *Quart. J. Roy. Meteor. Soc.*, **120**, 1111–1143, https://doi.org/10.1002/qj.49712051902.

Emmenegger, T., Y.-H. Kuo, S. Xie, C. Zhang, C. Tao, and J. D. Neelin, 2022: Evaluating tropical precipitation relations in CMIP6 models with ARM data. *J. Climate*, **35**, 6343–6360, https://doi.org/10.1175/JCLI-D-21-0386.1.

Fuchs-Stone, Ž., D. J. Raymond, and S. Sentić, 2020: OTREC2019: Convection over the East Pacific and southwest Caribbean. *Geophys. Res. Lett.*, **47**, e2020GL087564, https://doi.org/10.1029/2020GL087564.

Gaustad, K., and L. Riihimaki, 1998: MWR retrievals (MWRRET1LILJCLOU), 1999-01-01 to 2008-12-31, Tropical Western Pacific (TWP) Central Facility, Nauru Island (C2) (updated hourly). ARM Climate Research Facility Data Archive, accessed 13 August 2019, https://doi.org/10.5439/1027369.

Giangrande, S. E., and Coauthors, 2016: Convective cloud vertical velocity and mass-flux characteristics from radar wind profiler observations during GoAmazon2014/5. *J. Geophys. Res. Atmos.*, **121**, 12 891–12 913, https://doi.org/10.1002/2016JD025303.

Gjorgjievska, S., and D. J. Raymond, 2014: Interaction between dynamics and thermodynamics during tropical cyclogenesis. *Atmos. Chem. Phys.*, **14**, 3065–3082, https://doi.org/10.5194/acp-14-3065-2014.

Hajima, T., and Coauthors, 2019: MIROC MIROC-ES2L model output prepared for CMIP6 CMIP historical. Earth System Grid Federation, accessed 22 May 2020, https://doi.org/10.22033/ESGF/CMIP6.5602.

Hersbach, H., and Coauthors, 2020: The ERA5 global reanalysis. *Quart. J. Roy. Meteor. Soc.*, **146**, 1999–2049, https://doi.org/10.1002/qj.3803.

Hohenegger, C., and B. Stevens, 2013: Preconditioning deep convection with cumulus congestus. *J. Atmos. Sci.*, **70**, 448–464, https://doi.org/10.1175/JAS-D-12-089.1.

Holloway, C. E., and J. D. Neelin, 2009: Moisture vertical structure, column water vapor, and tropical deep convection. *J. Atmos. Sci.*, **66**, 1665–1683, https://doi.org/10.1175/2008JAS2806.1.

——, and ——, 2010: Temporal relations of column water vapor and tropical precipitation. *J. Atmos. Sci.*, **67**, 1091–1105, https://doi.org/10.1175/2009JAS3284.1.

Hourdin, F., and Coauthors, 2013: LMDZ5B: The atmospheric component of the IPSL climate model with revisited parameterizations for clouds and convection. *Climate Dyn.*, **40**, 2193–2222, https://doi.org/10.1007/s00382-012-1343-y.

Jensen, M. P., and A. D. Del Genio, 2006: Factors limiting convective cloud-top height at the ARM Nauru island climate research facility. *J. Climate*, **19**, 2105–2117, https://doi.org/10.1175/JCLI3722.1.

Jing, X., K. Suzuki, H. Guo, D. Goto, T. Ogura, T. Koshiro, and J. Mülmenstädt, 2017: A multimodel study on warm precipitation biases in global models compared to satellite

observations. *J. Geophys. Res. Atmos.*, **122**, 11 806–11 824, https://doi.org/10.1002/2017JD027310.

Kain, J. S., and J. M. Fritsch, 1990: A one-dimensional entraining/detraining plume model and its application in convective parameterization. *J. Atmos. Sci.*, **47**, 2784–2802, https://doi.org/10.1175/1520-0469(1990)047<2784:AODEPM>2.0.CO;2.

Keil, C., F. Heinlein, and G. C. Craig, 2014: The convective adjustment time-scale as indicator of predictability of convective precipitation. *Quart. J. Roy. Meteor. Soc.*, **140**, 480–490, https://doi.org/10.1002/qj.2143.

Kim, D., A. H. Sobel, A. D. Del Genio, Y. Chen, S. J. Camargo, M.-S. Yao, M. Kelley, and L. Nazarenko, 2012: The tropical subseasonal variability simulated in the NASA GISS general circulation model. *J. Climate*, **25**, 4641–4659, https://doi.org/10.1175/JCLI-D-11-00447.1.

——, A. D. Del Genio, and M.-S. Yao, 2013: Moist convection scheme in model E2. arXiv, 1312.7496v1, https://doi.org/10.48550/arXiv.1312.7496.

Kumar, V. V., C. Jakob, A. Protat, C. R. Williams, and P. T. May, 2015: Mass-flux characteristics of tropical cumulus clouds from wind profiler observations at Darwin, Australia. *J. Atmos. Sci.*, **72**, 1837–1855, https://doi.org/10.1175/JAS-D-14-0259.1.

Kuo, Y.-H., J. D. Neelin, and K. A. Schiro, 2018: Convective transition statistics over tropical oceans for climate model diagnostics: Observational baseline. *J. Atmos. Sci.*, **75**, 1553–1570, https://doi.org/10.1175/JAS-D-17-0287.1.

——, and Coauthors, 2020: Convective transition statistics over tropical oceans for climate model diagnostics: GCM evaluation. *J. Atmos. Sci.*, **77**, 379–403, https://doi.org/10.1175/JAS-D-19-0132.1.

Luo, Z. J., G. Y. Liu, and G. L. Stephens, 2010: Use of A-Train data to estimate convective buoyancy and entrainment rate. *Geophys. Res. Lett.*, **37**, L09804, https://doi.org/10.1029/2010GL042904.

Maloney, E. D., Á. F. Adames, and H. X. Bui, 2019: Madden–Julian oscillation changes under anthropogenic warming. *Nat. Climate Change*, **9**, 26–33, https://doi.org/10.1038/s41558-018-0331-6.

Manabe, S., and R. F. Strickler, 1964: Thermal equilibrium of the atmosphere with a convective adjustment. *J. Atmos. Sci.*, **21**, 361–385, https://doi.org/10.1175/1520-0469(1964)021<0361:TEOTAW>2.0.CO;2.

——, J. Smagorinsky, and R. F. Strickler, 1965: Simulated climatology of a general circulation model with a hydrologic cycle. *Mon. Wea. Rev.*, **93**, 769–798, https://doi.org/10.1175/1520-0493(1965)093<0769:SCOAGC>2.3.CO;2.

Mapes, B., and R. Neale, 2011: Parameterizing convective organization to escape the entrainment dilemma. *J. Adv. Model. Earth Syst.*, **3**, M06004, https://doi.org/10.1029/2011MS000042.

McGee, C. J., and S. C. van den Heever, 2014: Latent heating and mixing due to entrainment in tropical deep convection. *J. Atmos. Sci.*, **71**, 816–832, https://doi.org/10.1175/JAS-D-13-0140.1.

Meehl, G. A., W. D. Collins, B. A. Boville, J. T. Kiehl, T. M. L. Wigley, and J. M. Arblaster, 2000: Response of the NCAR climate system model to increased CO_2 and the role of physical processes. *J. Climate*, **13**, 1879–1898, https://doi.org/10.1175/1520-0442(2000)013<1879:ROTNCS>2.0.CO;2.

Möbis, B., and B. Stevens, 2012: Factors controlling the position of the intertropical convergence zone on an aquaplanet. *J. Adv. Model. Earth Syst.*, **4**, M00A04, https://doi.org/10.1029/2012MS000199.

Moorthi, S., and M. J. Suarez, 1992: Relaxed Arakawa-Schubert: A parameterization of moist convection for general circulation models. *Mon. Wea. Rev.*, **120**, 978–1002, https://doi.org/10.1175/1520-0493(1992)120<0978:RASAPO>2.0.CO;2.

NASA Goddard Institute for Space Studies, 2018: NASA-GISS GISS-E2.1G model output prepared for CMIP6 CMIP historical. Earth System Grid Federation, accessed 22 May 2020, https://doi.org/10.22033/ESGF/CMIP6.7127.

Neale, R. B., J. H. Richter, and M. Jochum, 2008: The impact of convection on ENSO: From a delayed oscillator to a series of events. *J. Climate*, **21**, 5904–5924, https://doi.org/10.1175/2008JCLI2244.1.

——, and Coauthors, 2010: Description of the NCAR Community Atmosphere Model (CAM 5.0). NCAR Tech. Note NCAR/TN-486+STR, 268 pp., www.cesm.ucar.edu/models/cesm1.1/cam/docs/description/cam5_desc.pdf.

Neelin, J. D., and J.-Y. Yu, 1994: Modes of tropical variability under convective adjustment and the Madden-Julian oscillation. Part I: Analytical results. *J. Atmos. Sci.*, **51**, 1876–1894, https://doi.org/10.1175/1520-0469(1994)051<1876:MOTVUC>2.0.CO;2.

——, and N. Zeng, 2000: A quasi-equilibrium tropical circulation model—formulation. *J. Atmos. Sci.*, **57**, 1741–1766, https://doi.org/10.1175/1520-0469(2000)057<1741:AQETCM>2.0.CO;2.

——, O. Peters, J. W.-B. Lin, K. Hales, and C. E. Holloway, 2008: Rethinking convective quasi-equilibrium: Observational constraints for stochastic convective schemes in climate models. *Philos. Trans. Roy. Soc.*, **A366**, 2579–2602, https://doi.org/10.1098/rsta.2008.0056.

——, ——, and K. Hales, 2009: The transition to strong convection. *J. Atmos. Sci.*, **66**, 2367–2384, https://doi.org/10.1175/2009JAS2962.1.

Norris, J., A. Hall, J. D. Neelin, C. W. Thackeray, and D. Chen, 2021: Evaluation of the tail of the probability distribution of daily and sub-daily precipitation in CMIP6 models. *J. Climate*, **34**, 2701–2721, https://doi.org/10.1175/JCLI-D-20-0182.1.

Pall, P., M. R. Allen, and D. A. Stone, 2007: Testing the Clausius-Clapeyron constraint on changes in extreme precipitation under CO_2 warming. *Climate Dyn.*, **28**, 351–363, https://doi.org/10.1007/s00382-006-0180-2.

Peters, O., and J. D. Neelin, 2006: Critical phenomena in atmospheric precipitation. *Nat. Phys.*, **2**, 393–396, https://doi.org/10.1038/nphys314.

Powell, S. W., 2022: Criticality in the shallow-to-deep transition of simulated tropical marine convection. *J. Atmos. Sci.*, **79**, 1805–1819, https://doi.org/10.1175/JAS-D-21-0155.1.

Raymond, D. J., 1994: Cumulus convection and the Madden-Julian oscillation of the tropical troposphere. *Physica D*, **77** (1–3), 1–22, https://doi.org/10.1016/0167-2789(94)90124-4.

——, 1995: Regulation of moist convection over the West Pacific warm pool. *J. Atmos. Sci.*, **52**, 3945–3959, https://doi.org/10.1175/1520-0469(1995)052<3945:ROMCOT>2.0.CO;2.

——, 2017: Convection in the East Pacific intertropical convergence zone. *Geophys. Res. Lett.*, **44**, 562–568, https://doi.org/10.1002/2016GL071554.

——, G. Raga, C. S. Bretherton, J. Molinari, C. López-Carrillo, and Ž. Fuchs, 2003: Convective forcing in the intertropical convergence zone of the eastern Pacific. *J. Atmos. Sci.*, **60**, 2064–2082, https://doi.org/10.1175/1520-0469(2003)060<2064:CFITIC>2.0.CO;2.

——, S. L. Sessions, and C. López Carrillo, 2011: Thermodynamics of tropical cyclogenesis in the northwest Pacific. *J. Geophys. Res.*, **116**, D18101, https://doi.org/10.1029/2011JD015624.

Rio, C., F. Hourdin, J.-Y. Grandpeix, and J.-P. Lafore, 2009: Shifting the diurnal cycle of parameterized deep convection over land. *Geophys. Res. Lett.*, **36**, L07809, https://doi.org/10.1029/2008GL036779.

Rushley, S. S., D. Kim, C. S. Bretherton, and M.-S. Ahn, 2018: Reexamining the nonlinear moisture-precipitation relationship over the tropical oceans. *Geophys. Res. Lett.*, **45**, 1133–1140, https://doi.org/10.1002/2017GL076296.

Sarachik, E. S., 1985: A simple theory for the vertical structure of the tropical atmosphere. *Pure Appl. Geophys.*, **123**, 261–271, https://doi.org/10.1007/BF00877022.

Schiro, K. A., 2017: Thermodynamic controls on deep convection in the tropics: Observations and applications to modeling. Ph.D. dissertation, University of California, 149 pp.

——, J. D. Neelin, D. K. Adams, and B. R. Lintner, 2016: Deep convection and column water vapor over tropical land versus tropical ocean: A comparison between the Amazon and the tropical western Pacific. *J. Atmos. Sci.*, **73**, 4043–4063, https://doi.org/10.1175/JAS-D-16-0119.1.

——, F. Ahmed, S. E. Giangrande, and J. D. Neelin, 2018: GoAmazon2014/5 campaign points to deep-inflow approach to deep convection across scales. *Proc. Natl. Acad. Sci. USA*, **115**, 4577–4582, https://doi.org/10.1073/pnas.1719842115.

Schmidt, G. A., and Coauthors, 2014: Configuration and assessment of the GISS ModelE2 contributions to the CMIP5 archive. *J. Adv. Model. Earth Syst.*, **6**, 141–184, https://doi.org/10.1002/2013MS000265.

Schneider, T., P. A. O'Gorman, and X. J. Levine, 2010: Water vapor and the dynamics of climate changes. *Rev. Geophys.*, **48**, RG3001, https://doi.org/10.1029/2009RG000302.

Seland, Ø., and Coauthors, 2019: NCC NorESM2-LM model output prepared for CMIP6 CMIP historical. Earth System Grid Federation, accessed 22 May 2020, https://doi.org/10.22033/ESGF/CMIP6.8036.

——, and Coauthors, 2020: Overview of the Norwegian Earth System Model (NorESM2) and key climate response of CMIP6 DECK, historical, and scenario simulations. *Geosci. Model Dev.*, **13**, 6165–6200, https://doi.org/10.5194/gmd-13-6165-2020.

Singh, M. S., and P. A. O'Gorman, 2013: Influence of entrainment on the thermal stratification in simulations of radiative-convective equilibrium. *Geophys. Res. Lett.*, **40**, 4398–4403, https://doi.org/10.1002/grl.50796.

——, and S. Neogi, 2022: On the interaction between moist convection and large-scale ascent in the tropics. *J. Climate*, **35**, 4417–4435, https://doi.org/10.1175/JCLI-D-21-0717.1.

——, R. A. Warren, and C. Jakob, 2019: A steady-state model for the relationship between humidity, instability, and precipitation in the tropics. *J. Adv. Model. Earth Syst.*, **11**, 3973–3994, https://doi.org/10.1029/2019MS001686.

Sobel, A. H., and C. S. Bretherton, 2000: Modeling tropical precipitation in a single column. *J. Climate*, **13**, 4378–4392, https://doi.org/10.1175/1520-0442(2000)013<4378:MTPIAS>2.0.CO;2.

Stephens, G. L., and Coauthors, 2010: Dreary state of precipitation in global models. *J. Geophys. Res.*, **115**, D24211, https://doi.org/10.1029/2010JD014532.

Stevens, B., and A. P. Siebesma, 2020: Clouds as fluids. *Clouds and Climate: Climate Science's Greatest Challenge*, A. Siebesma et al., Eds., Cambridge University Press, 35–73.

——, H. Brogniez, C. Kiemle, J.-L. Lacour, C. Crevoisier, and J. Kiliani, 2017: Structure and dynamical influence of water vapor in the lower tropical troposphere. *Shallow Clouds, Water Vapor, Circulation, and Climate Sensitivity*, R. Pincus et al., Eds., Space Sciences Series, Vol. 65, Springer, 199–225.

Tang, S., P. Gleckler, S. Xie, J. Lee, M.-S. Ahn, C. Covey, and C. Zhang, 2021: Evaluating the diurnal and semidiurnal cycle of precipitation in CMIP6 models using satellite-and ground-based observations. *J. Climate*, **34**, 3189–3210, https://doi.org/10.1175/JCLI-D-20-0639.1.

——, and Coauthors, 2022: Long-term single-column model intercomparison of diurnal cycle of precipitation over midlatitude and tropical land. *Quart. J. Roy. Meteor. Soc.*, **148**, 641–669, https://doi.org/10.1002/qj.4222.

Tatebe, H., and M. Watanabe, 2018: MIROC MIROC6 model output prepared for CMIP6 CMIP historical. Earth System Grid Federation, accessed 22 May 2020, https://doi.org/10.22033/ESGF/CMIP6.5603.

Tokioka, T., K. Yamazaki, A. Kitoh, and T. Ose, 1988: The equatorial 30–60 day oscillation and the Arakawa-Schubert penetrative cumulus parameterization. *J. Meteor. Soc. Japan*, **66**, 883–901, https://doi.org/10.2151/jmsj1965.66.6_883.

Trenberth, K. E., A. Dai, R. M. Rasmussen, and D. B. Parsons, 2003: The changing character of precipitation. *Bull. Amer. Meteor. Soc.*, **84**. 1205–1218, https://doi.org/10.1175/BAMS-84-9-1205.

Tropical Rainfall Measuring Mission, 2011: TRMM (TMPA) rainfall estimate L3 3 hour 0.25 degree × 0.25 degree v7 (TRMM_3B42). Goddard Earth Sciences Data and Information Services Center, accessed 22 May 2020, https://disc.gsfc.nasa.gov/datasets/TRMM_3B42_7/summary/.

Waite, M. L., and B. Khouider, 2010: The deepening of tropical convection by congestus preconditioning. *J. Atmos. Sci.*, **67**, 2601–2615, https://doi.org/10.1175/2010JAS3357.1.

Wieners, K.-H., and Coauthors, 2019: MPI-M MPI-ESM1.2-LR model output prepared for CMIP6 CMIP historical. Earth System Grid Federation, accessed 22 May 2020, https://doi.org/10.22033/ESGF/CMIP6.6595.

Wolding, B., J. Dias, G. Kiladis, F. Ahmed, S. W. Powell, E. Maloney, and M. Branson, 2020: Interactions between moisture and tropical convection. Part I: The coevolution of moisture and convection. *J. Atmos. Sci.*, **77**, 1783–1799, https://doi.org/10.1175/JAS-D-19-0225.1.

——, S. W. Powell, F. Ahmed, J. Dias, M. Gehne, G. Kiladis, and J. D. Neelin, 2022: Tropical thermodynamic–convection coupling in observations and reanalyses. *J. Atmos. Sci.*, **79**, 1781–1803, https://doi.org/10.1175/JAS-D-21-0256.1.

Xie, S., and Coauthors, 2010: Clouds and more: ARM climate modeling best estimate data. *Bull. Amer. Meteor. Soc.*, **91**, 13–20, https://doi.org/10.1175/2009BAMS2891.1.

——, and Coauthors, 2019: Improved diurnal cycle of precipitation in E3SM with a revised convective triggering function. *J. Adv. Model. Earth Syst.*, **11**, 2290–2310, https://doi.org/10.1029/2019MS001702.

Xu, K.-M., and D. A. Randall, 2001: Updraft and downdraft statistics of simulated tropical and midlatitude cumulus convection. *J. Atmos. Sci.*, **58**, 1630–1649, https://doi.org/10.1175/1520-0469(2001)058<1630:UADSOS>2.0.CO;2.

Yang, D., W. Zhou, and S. D. Seidel, 2022: Substantial influence of vapour buoyancy on tropospheric air temperature and subtropical cloud. *Nat. Geosci.*, **15**, 781–788, https://doi.org/10.1038/s41561-022-01033-x.

Yano, J.-I., and R. S. Plant, 2012: Convective quasi-equilibrium. *Rev. Geophys.*, **50**, RG4004, https://doi.org/10.1029/2011RG000378.

Yeo, K., and D. M. Romps, 2013: Measurement of convective entrainment using Lagrangian particles. *J. Atmos. Sci.*, **70**, 266–277, https://doi.org/10.1175/JAS-D-12-0144.1.

Yukimoto, S., and Coauthors, 2011: Meteorological Research Institute-Earth System Model version 1 (MRI-ESM1)-model description. Meteorological Research Institute Tech. Rep. 64, 96 pp., https://www.mri-jma.go.jp/Publish/Technical/DATA/VOL_64/tec_rep_mri_64.pdf.

——, and Coauthors, 2019: MRI MRI-ESM2.0 model output prepared for CMIP6 CMIP historical. Earth System Grid Federation, accessed 22 May 2020, https://doi.org/10.22033/ESGF/CMIP6.6842.

Zhang, G. J., 2009: Effects of entrainment on convective available potential energy and closure assumptions in convection parameterization. *J. Geophys. Res.*, **114**, D07109, https://doi.org/10.1029/2008JD010976.

——, and N. A. McFarlane, 1995: Role of convective scale momentum transport in climate simulation. *J. Geophys. Res.*, **100**, 1417–1426, https://doi.org/10.1029/94JD02519.

Zhang, Y., and S. A. Klein, 2010: Mechanisms affecting the transition from shallow to deep convection over land: Inferences from observations of the diurnal cycle collected at the ARM Southern Great Plains site. *J. Atmos. Sci.*, **67**, 2943–2959, https://doi.org/10.1175/2010JAS3366.1.

Zhou, W., and S.-P. Xie, 2019: A conceptual spectral plume model for understanding tropical temperature profile and convective updraft velocities. *J. Atmos. Sci.*, **76**, 2801–2814, https://doi.org/10.1175/JAS-D-18-0330.1.

Zhu, H., and H. H. Hendon, 2015: Role of large-scale moisture advection for simulation of the MJO with increased entrainment. *Quart. J. Roy. Meteor. Soc.*, **141**, 2127–2136, https://doi.org/10.1002/qj.2510.

Zuidema, P., G. Torri, C. Muller, and A. Chandra, 2017: A survey of precipitation-induced atmospheric cold pools over oceans and their interactions with the larger-scale environment. *Surv. Geophys.*, **38**, 1283–1305, https://doi.org/10.1007/s10712-017-9447-x.

Supplemental Material

Journal of Climate
The Physics behind Precipitation Onset Bias in CMIP6 Models: The Pseudo-Entrainment Diagnostic and Trade-Offs between Lapse Rate and Humidity
https://doi.org/10.1175/JCLI-D-23-0227.1

The physics behind precipitation onset bias in CMIP6 models: the pseudo-entrainment diagnostic and trade-offs between lapse rate and humidity: Supplemental Material

Todd Emmenegger,[a] Fiaz Ahmed, [a] Yi-Hung Kuo, [a,b] Shaocheng Xie, [c] Chengzhu Zhang, [c] Cheng Tao, [c] J. David Neelin, [a]

[a] *Department of Atmospheric and Oceanic Sciences, University of California, Los Angeles, Los Angeles, CA*
[b] *Cooperative Institute for Modeling the Earth System, Program in Oceanic and Atmospheric Sciences, Princeton University, Princeton, NJ*
[c] *Lawrence Livermore National Laboratory, Livermore, California*

1. Equivalent Potential Temperature Definition of Buoyancy

The following derivation closely resembles that of Adames et al. (2021) Appendix A, but uses a constant reference in it θ_{es} approximation. A more detailed derivation of Equivalent Potential Temperature and parcel buoyancy may be found in Raymond (1994) Section 2 - 2.1.

We begin with the approximation to virtual temperature, T_v,

$$T_v \approx (1+0.61q_v - q_c)T$$

where T is the temperature, and q_v and q_c are the vapor and condensate mixing ratios respectively. We write a small change in T_v as

$$\delta T_v \approx (1+0.61q_v - q_c)\delta T + (0.61\delta q_v - \delta q_c)T \tag{1}$$

We can rewrite the virtual temperature definition of buoyancy,

$$B = g\left[\frac{\delta T_v}{T_v}\right]$$

using 1 as

$$B = g\left[\frac{\delta T}{T} + \frac{0.61\delta q_v - \delta q_c}{1+0.61q_v - q_c}\right] \tag{2}$$

With $0.61q_v - q_c << 1$, $(1+0.61q_v - q_c)^{-1} \approx 1 - 0.61q_v + q_c$, the expression for buoyancy is simplified to

$$B = g\left[\frac{\delta T}{T} + 0.61\delta q_v - \delta q_c\right] \tag{3}$$

where second-order terms have been dropped.

We will rewrite the fractional temperature difference of B in terms of a equivalent saturation potential temperature, θ_{es}, a variable conserved in a saturated parcel with respect to moist adiabatic motions. Consider the approximate definition of equivalent potential temperature, θ_{es}:

$$\theta_{es} = \theta \exp\left[\frac{Lq_s}{c_p T_0}\right]$$

where θ is the potential temperature, L is the latent heat of vaporization, q_s is the saturation mixing ratio, c_p is the specific heat capacity of dry air, and T_0 is a reference temperature.

For simplicity, define θ_{es} as functional:

$$\theta_{es} \equiv \theta_{es}[\theta(p,T), \xi(q_s(T);T_0)] = \theta\xi$$

where

$$\xi = \exp\left[\frac{Lq_s}{c_p T_0}\right]$$

.

Differentiating,

$$\delta\theta_{es} = \frac{\partial\theta_{es}}{\partial\theta}\frac{\partial\theta}{\partial T}\delta T + \frac{\partial\theta_{es}}{\partial\xi}\frac{d\xi}{dq_s}\frac{dq_s}{dT}\delta T$$

$$= \frac{\xi\theta}{T}\delta T + \theta\xi\frac{L}{c_p T_0}\frac{Lq_s}{R_v T^2}\delta T$$

then,

$$\frac{\delta\theta es}{\theta_{es}} = \frac{\delta T}{T}\left(1 + \frac{L^2 q_s}{c_p R_v T_0 T}\right)$$

$$\frac{\delta\theta es}{\kappa\theta_{es}} = \frac{\delta T}{T} \tag{4}$$

Using (4) in the virtual temperature definition of buoyancy, (3) gives the final form of buoyancy used in the

Corresponding author: Todd Emmenegger, temmen@atmos.ucla.edu

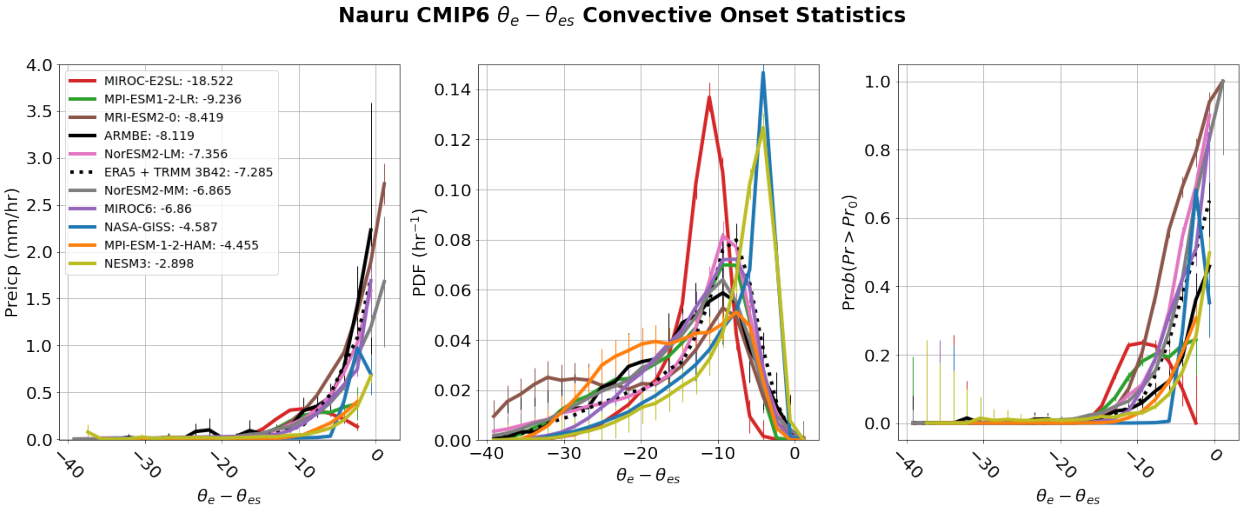

Fig. S1. Similar to Figure 3 of the main text but statistics are conditioned on average LFT subsaturation, $\theta_e - \theta_{es}$ averaged over 900 - 750 hPa.

manuscript,

$$B = g\left[\frac{\delta\theta es}{\kappa\theta_{es}} + 0.61\delta q_v - \delta q_c\right]$$

2. Convective onset statistics as a function of LFT subsaturation

Figure S1 is provided for comparison to Fig. 3 in the main text which shows convective onset statistics as a function of B_L. Similarities between these figures illustrate the importance of lower free troposphere (LFT) subsaturation to the convective onset.

References

Adames, Á. F., Powell, S. W., Ahmed, F., Mayta, V. C., and Neelin, J. D. (2021). Tropical precipitation evolution in a buoyancy-budget framework. *Journal of the Atmospheric Sciences*, 78(2):509–528.

Raymond, D. J. (1994). Cumulus convection and the madden-julian oscillation of the tropical troposphere. *Physica D: Nonlinear Phenomena*, 77(1-3):1–22.